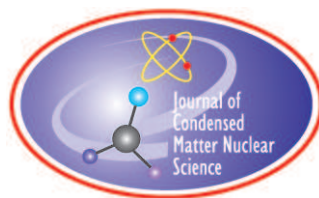


JOURNAL OF CONDENSED MATTER NUCLEAR SCIENCE

Experiments and Methods in Cold Fusion

VOLUME 40, November 2025



JOURNAL OF CONDENSED MATTER NUCLEAR SCIENCE

Experiments and Methods in Cold Fusion

Editor-in-Chief

Jean-Paul Biberian
Marseille, France

Editorial Board

Peter Hagelstein
MIT, USA

Xing Zhong Li
Tsinghua University, China

Edmund Storms
KivaLabs, LLC, USA

George Miley
*Fusion Studies Laboratory,
University of Illinois, USA*

Michael McKubre
SRI International, USA

JOURNAL OF CONDENSED MATTER NUCLEAR SCIENCE

Volume 40, November 2025

© 2025 ISCMNS. All rights reserved. ISSN 2227-3123

This journal and the individual contributions contained in it are protected under copyright by ISCMNS and the following terms and conditions apply.

Electronic usage or storage of data

JCMNS is an open-access scientific journal and no special permissions or fees are required to download for personal non-commercial use or for teaching purposes in an educational institution.

All other uses including printing, copying, distribution require the written consent of ISCMNS.

Permission of the ISCMNS and payment of a fee are required for photocopying, including multiple or systematic copying, copying for advertising or promotional purposes, resale, and all forms of document delivery.

Permissions may be sought directly from ISCMNS, E-mail: CMNSEditor@iscmns.org. For further details you may also visit our web site: <http://www.iscmns.org/CMNS/>

Members of ISCMNS may reproduce the table of contents or prepare lists of articles for internal circulation within their institutions.

Orders, claims, author inquiries and journal inquiries

Please contact the Editor in Chief, CMNSEditor@iscmns.org or webmaster@iscmns.org



JOURNAL OF CONDENSED MATTER NUCLEAR SCIENCE

Volume 40

2025

CONTENTS

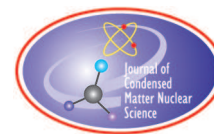
RESEARCH ARTICLES

- On the Exothermic Response Frequencies When PdD Is Subjected to coherent THz Radiation 1
J. S. Brown
- Random Thermal Spikes Observed in 99% Palladium – 1% Uranium Alloy Foil Electrolytically Charged with Deuterium: Confirmation of Solid-State Fusion 6
Douglas A. Pinnow and Kirk Miller
- Thermodynamics in Lattice Assisted Nuclear Reactions 21
Mitchell R. Swartz, ScD, EE, MD
- The Use of Graphene for Controlled LENR in Thin Conductive Targets via Optimized Low-Voltage Corona Discharge 40
V. I. Vysotskii, M. V. Vysotsky, and S. Bartalucci
- Stimulation of Efficient Low Energy Tritium Fusion Under The Action of a Weak Undamped Thermal Wave on Remote TiD Target 48
Vladimir I. Vysotskii, Alla A. Kornilova, and Sergey N. Gaydamaka

Preface

This new volume 40 includes 5 experimental and theoretical articles. It is always for me a great joy to see that scientists all around the world are working together to discover the mysteries of Low Energy Nuclear Reactions. After more than 36 years since the announcement by Professors Martin Fleischman and Stanley Pons, we are still trying to find out what is happening in metals loaded with hydrogen. We need more experimental data so that theoreticians can develop good models.

After so many years of basic research, we see now several start-up companies in the process of bringing a commercial product on market. This is of prime importance, since, the scientists world-wide do not accept this new field as genuine. At this point in time, a demonstrator will be the key to open the door to make Cold Fusion a reality.



Research Article

On the Exothermic Response Frequencies When PdD Is Subjected to coherent THz Radiation

J. S. Brown

Abstract

In this paper we identify the three specific frequencies in the 3–25 THz range that have been found to trigger anomalous exothermy in PdD with low-lying dipole transitions in the spectrum of a single deuteron trapped at the octahedral site. We speculate that the state phase coherence that characterizes the ground state of the Tavis-Cummings Hamiltonian may give rise to an increase in the rate of deuteron-deuteron fusion over that of stochastic deuterons.

© 2025 ICCF. All rights reserved. ISSN 2227-3123

Keywords: PdD, Deuteron vibrational spectrum, Dipole-photon coupling Tavis-Cummings, Collective oscillation

1. Introduction

In a series of really quite remarkable experiments, Letts and Hagelstein [1] succeeded in triggering an anomalous exothermy in ($PdD_{0.9}$) by means of laser radiation tuned to three specific infra-red frequencies in the range 3–24 THz. The frequency selectivity (Q-value) of the anomalies were in the range of 14–39, suggesting a lightly damped and narrow-band resonance response of the target material. Hagelstein has put forward an explanations for the exothermy based on the fact that the two lower response frequencies correspond to points of zero group velocity in the optical phonon bands, but he has been unable to account for the other (stronger) response at 21 THz. We however question his phonon-band interpretation because zero group velocity implies zero propagation of energy along the chain of oscillators. Indeed we question whether it is even possible to speak of phonon bands when a significant percentage of the sites are vacant.

We are unaware of any other credible attempts to explain this remarkable phenomenon and attribute this to a general scepticism regarding the calorimetric data that we certainly do not share. In this paper we draw attention to the fact that all of the observed exothermic response frequencies correspond to low-lying dipolar transitions in the vibration spectrum of individual noninteracting trapped deuterons. We then point out that when the laser radiation is of sufficient intensity, all of the deuterons will cohere in a long-lived Dicke ground state and that this would lead to an enhancement of the normally negligible deuteron-fusion rate by a factor equal to the number of deuteron neighbours.

2. Laser-Deuteron Interaction Hamiltonian

We are going to make several simplifying assumptions. The first of these is that the laser radiation frequency ω excites transitions between a single pair of states in the deuteron vibrational spectrum (with $|E_i - E_j| = \hbar\omega$) and that the plane of polarization is along one of the fcc axes, which we will label x .

According to the Drude model [2], the complex refractive index of Pd at THz frequencies is given approximately by:

$$\epsilon = 1 - \frac{\omega_P^2}{\gamma^2 + \omega^2} + \frac{\omega_P^2 \gamma}{\omega(\gamma^2 + \omega^2)} i \quad (1)$$

implying

$$\sqrt{2}n = \sqrt{|\epsilon| + \text{Re}\{\epsilon\}} + \sqrt{|\epsilon| - \text{Re}\{\epsilon\}} i \quad (2)$$

Using $\hbar\omega_P = 2.77$ eV and $\hbar\gamma = 0.068$ eV as published in [3], n at 10 THz $\approx 24 + 43i$. This means that the laser radiation only penetrates to a depth of around one micron.

Within this surface layer, we envisage N deuterons occupying an equal number of interstitial sites of octahedral symmetry. In other words, we assume stoichiometry and translational invariance.

An assembly of non-interacting two-state quasi atoms driven resonantly by a field of coherent radiation is most simply modelled by the Tavis-Cummings Hamiltonian in which the 2^N state space is transformed into that of a single quasi-spin multiplet. Following [4] and [5] we have

$$H_{TC} = \hbar\omega a^\dagger a + \hbar\omega \left[\frac{N}{2} + S_3 \right] + g (a^\dagger S_+ + a S_-) \quad (3)$$

The sum of the number of photons and excited sites is a conserved quantity (N_{exc}) and the energy levels are given by

$$E_j = N_{exc} \hbar\omega + 2jg \sqrt{N_{exc}} \quad (4)$$

where $-N/2 \leq j \leq N/2$.

The lowest energy is clearly $E_{-N/2} = N_{exc} \hbar\omega - Ng \sqrt{N_{exc}}$ and the gap between levels is $\Delta E = g \sqrt{N_{exc}}$. The field amplitude E_0 of a single photon over N sites each of volume Ω is given by

$$\hbar\omega = 2n^2 \epsilon_0 E_0^2 N \Omega \quad (5)$$

where n is the real part of the refractive index at ω .

In a surface layer of depth $\lambda/2$, the coupling to the E-field will vary strongly with position, being greatest for sites at the centre of the layer, but the mean photon-site coupling is approximately described by

$$g_{ij}^2 = e^2 E_0^2 |\langle i|x|j \rangle|^2 = \frac{e^2 |\langle i|x|j \rangle|^2 \hbar\omega}{2Nn^2 \Omega \epsilon_0} \quad (6)$$

3. Palladium Deuteride

Palladium is one of several transition metals that can reversibly absorb hydrogen up to the point of stoichiometry, in which every available interstitial site of octahedral (O) symmetry is occupied by a hydrogen nucleus. As pointed out above, the large mass ratio between the hydrogen nucleus and the host atoms, means that the quantum oscillation is decoupled from the motion of host atoms and the interstitial hydrogen nucleus (p, D) experiences an effective static potential, with local minima at the octahedral and tetragonal symmetry points. Furthermore, each deuteron is screened

by the Fermi gas such that intersite deuteron-deuteron interactions are small. The screened deuterons are effectively almost neutral particles, resulting in high mobility within the lattice and a very shallow effective potential. As a consequence, even the ground state has a substantial spatial extent on the order of 0.2\AA .

A single deuteron in such an environment exhibits a spectrum of singlet, doublet and triplet state representations of the local point symmetry group. The ground state is a singlet with even parity about the minimum potential along each of the symmetry axes. The next level is a triplet of states with odd parity along one of the symmetry axes and an excitation energy of the order of 0.04 eV ($\approx 10\text{ THz}$). The real and imaginary parts of the refractive index are comparable in this part of the spectrum, so there is effectively only one internally reflected mode along each of the x , y and z axes, and a single photon is effectively normalized to a slab volume $A\lambda/2$. We conclude that microlayers of non-stoichiometric PdD are amenable to the Tavis-Cummings model in which a single photon mode is coupled to N identical two-level quasi-atoms.

In PdD, each interstitial octahedral site corresponds to a volume $\Omega = \frac{1}{4}a^3 \approx 1.6 \times 10^{-29}\text{ m}^3$, so

$$\frac{e^2}{\epsilon_0\Omega} \approx 1.1 \times 10^{21}\text{ eVm}^{-2} \quad (7)$$

and the dipole transition coupling coefficient is given by:

$$g_{ij}^2 \approx \frac{\hbar\omega_{ij} | \langle i|x|j \rangle |^2}{Nn^2} \times 5.5 \times 10^{20}\text{ eVm}^{-2} \quad (8)$$

We chose the x axis as our dipole and E-field direction, but exactly the same results would be obtained for y and z axes by virtue of the fcc point symmetry at the octahedral site. μ_x dipoles can only be formed by products of states that have opposite x -parity and equal y and z parities.

We solved the $[\cdot + \cdot]$ deuteron states on a 3-dimensional grid of pitch 0.25\AA using the semi-empirical effective potential published in [6] and were able to substantially confirm the findings of that paper. We checked all dipoles of states involving $[\cdot + \cdot]$, $[\cdot - \cdot]$, $[\cdot - \cdot]$, but none of these were larger than those involving $[\cdot + \cdot]$ parity states and they lie at higher energies, so we do not consider them here.

The energy levels E_i (relative to the potential minimum at the octahedral symmetry point) of the ten lowest states in each of the $[+++]$ and $[-++]$ subgroups are listed below:

i, j	$E_{i_{[+++]}} \times 10^{-3}\text{ eV}$	$E_{j_{[-++]}} \times 10^{-3}\text{ eV}$
0	47	88
1	138	173
2	190	190
3	217	213
4	148	248
5	148	182
6	233	283
7	233	283
8	283	277
9	284	289

$[+++]$ states $\{4, 5\}$ and $\{6, 7\}$ are degenerate doublets. None of lowest $10[-++]$ states are degenerate. The largest μ_x dipole elements are tabulated below, together with the dimensionless photon mode coupling constants $g_{ij}\sqrt{N}/(\hbar\omega)$:

$i_{[+++]}$	$j_{[+--]}$	$ E_i - E_j \times 10^{-3} \text{ eV}$	$= \text{THz}$	E_{lower}	$\langle i x j \rangle (\text{\AA})$	$g_{ij} \sqrt{N} / (\hbar\omega)$
0	0	40	9.8	47	0.16	0.08
1	3	74	18.0	138	0.10	0.07
2	8	87	21.1	190	0.08	0.07
3	1	45	10.8	173	0.17	0.09
3	6	66	15.9	217	0.12	0.08
4 + 5	3	65	15.7	148	0.19	0.11
6	5	51	12.4	182	0.14	0.08
6	9	56	13.6	233	0.15	0.09
7	5	51	12.4	182	0.14	0.08
7	9	56	13.6	233	0.15	0.09
9	3	72	17.3	213	0.12	0.09

Because the $[+++]$ parity states 4 and 5 are degenerate, we have added their dipole products with $[+ - +]$ state 3 in quadrature.

3.1. Second Order Effects

It should be understood that the above tabulations are first-order in the photon-dipole interaction. This rotating wave approximation (RWA) does not allow for the effects of virtual processes that transiently change the n_{exc} . There will also be second order effects on the transition frequencies arising from mixing with states that are higher up the excitation ladder. Interstitial hydrogen nuclei have a complex vibrational spectrum. Any correlation with the actual empirical response frequencies is hence going to be approximate and subject to error bars that are extremely hard to quantify.

4. Tentative Identification of the Response Frequencies

The 0-0 transition corresponds to the Γ point of the optical phonon band.

Comparison with Fig 10b of [1] leads us to make the tentative identifications (shown in bold) of the three responses observed at 8.3, 15.1 and 20.5 THz with the theoretical dipole transitions at 9.8, 15, 7 and 21.1 THz. Our second tabulated entry also predicts a strong dipole transition at 18.0 Thz that is not visible in the fitted curve of Fig 10b of [1]. However the raw data in their Table 1 does indeed show an observed exothermic response at 18.0 Thz, which was evidently overlooked in the curve fitting.

We can not exclude the possibility that the numerical correspondence noted above is merely a coincidence and that the actual mechanism for frequency-selective exothermic response has nothing to do with dipole transitions.

5. The Coherent N-Deuteron State

Every eigenstate of (3) comprises contributions from every one of the 2^N states of the deuterons. In the absence of intersite interactions, the lowest singlet eigenstate is the simple product of N one-particle wavefunctions:

$$\Psi(\mathbf{r}_1, \mathbf{r}_2, \dots, \mathbf{r}_k, \dots, \mathbf{r}_N) = \prod_{k=1}^N [c_i \psi_i(\mathbf{r}_k - \mathbf{R}_k) + c_j \psi_j(\mathbf{r}_k - \mathbf{R}_k)] \equiv \prod_{k=1}^N \psi_{ij}(\mathbf{r}_k - \mathbf{R}_k) \quad (9)$$

$$c_i^2 = \frac{1}{2} - \eta \text{ and } c_j^2 = \frac{1}{2} + \eta \quad \text{where } \lim_{N \rightarrow \infty} \eta(N) = 0 \quad (10)$$

The superposition mimics the classical response of charged monopoles oscillating about their equilibrium positions in synchronism with the applied oscillating E-field. The only other Tavis-Cummings state that is a simple product is

the highest. This state differs from the lowest state solely in regard to the sign of $\frac{c_j}{c_i}$. It corresponds to a vibration in counterphase to the E-field.

Realistically, the H_{TC} must be supplemented by an interaction potential $U(r)$ between neighbouring deuterons at sites with relative separation vectors $\mathbf{R}_k - \mathbf{R}_{k'} = \{0, \pm \frac{a}{2}, \pm \frac{a}{2}\}$ *et cycl.* This interaction is a modified Weidel-ThomasFermi potential for separations greater than the nuclear radius and an imaginary optical potential for subnuclear separation, as shown in Fig. 4 of [7]:

$$U(r) \approx \frac{e^2}{4\pi\epsilon_0 r} e^{-\kappa r} \cos \kappa r \text{ for } r > r_{\text{deut}} \quad (11)$$

$$U(r) = iW(r) \text{ for } r \leq r_{\text{deut}} \quad (12)$$

$U\left(\frac{a}{\sqrt{2}}\right) \approx 0.005$ eV so there is a small first-order energy shift (upwards) per site. The second-order modification of the pair wavefunction is negligible at the intersite separation. We can represent the perturbation in terms of an anti-correlation (attenuation) function $\phi(r)$ that is 1 at $r = a/2$ and which falls exponentially at $r \ll a$ as a result of the repulsive Coulomb interaction:

$$\psi_{ij}(\mathbf{r}_1, \mathbf{r}_2) = \psi_{ij}(\mathbf{r}_1 - \mathbf{R}_k) \psi_{ij}(\mathbf{r}_2 - \mathbf{R}_{k'}) \phi(|\mathbf{r}_1 - \mathbf{r}_2|) \quad (13)$$

For each pair of neighbours, the fusion rate is proportional to

$$\int d^3\mathbf{r}_1 \int_{|\mathbf{r}_1 - \mathbf{r}_2| < r_{\text{deut}}} \psi_{ij}^\dagger(\mathbf{r}_1, \mathbf{r}_2) W \psi_{ij}(\mathbf{r}_1, \mathbf{r}_2) d^3\mathbf{r}_2 \quad (14)$$

As is well-known and understood, this rate is vanishingly small because $U(r_{\text{deut}})$ is on the order of 100 KeV.

The energy gap to the next lowest level (an N-tuplet) of the (interaction modified) H_{TC} is $\sqrt{N_{\text{exc}}}/2g\hbar\omega$. In the experiments [1], N_{exc} was an unknown quantity because the THz radiation was produced from nonlinear mixing of the light from two red lasers and the efficiency of that mixing has not yet been ascertained. However we conclude from (4) that if the laser radiation is sufficiently strong, the thermodynamically favoured state of the N deuterons is one in which they occupy the lowest energy state described above, for times much longer than the vibrational period.

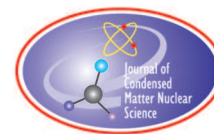
6. Further Work

State coherence per se should not have any effect on the fusion rate. However, if we consider the time-dependent Hamiltonian for two neighbouring deuterons in the coherent E-field, the transverse dipole-dipole interaction, which is intrinsically very small, is magnified by a factor $\sqrt{N_{\text{exc}}}$. This will lead to an effective attractive potential that at least partially cancels the Coulomb repulsion. I am currently working on an explicit calculation of this.

Fusion events arising out of this mechanism will be intrinsically delocalised over the coherence volume. No high energy fusion product, such as gamma rays, can emerge from such a volume on account of their tiny wavelength relative to the region of phase coherence. We conclude that the 24 MeV excitation will relax via a large number of low energy quanta, such as phonon excitations.

References

- [1] P. L. Hagelstein, D. Letts, and D. Cravens, J. Condensed Matter Nucl. Sci. 3, 59–76, (2010).
- [2] S. N. Rashkeev, et al., Zh. Eksp. Teor. Fiz. 88, 1687–1698 (1985).
- [3] A. Bolotin and T. P. Chukina, Opt. Spektrosk. 23, 620 (1967).
- [4] B. M. Garraway, Phil. Trans. R. Soc. A369, 1137–1155 (2011).
- [5] J. H. Zou et al., New J. Phys. 15, 123032 (2013).
- [6] H. Krimmel et al., J. Phys. Condens. Matter 6, 7679 (1994).
- [7] A. Takahashi, J. Condensed Matter Nucl. Sci. 19, 1–18 (2016).



Research Article

Random Thermal Spikes Observed in 99% Palladium – 1% Uranium Alloy Foil Electrolytically Charged with Deuterium: Confirmation of Solid-State Fusion

Douglas A. Pinnow* and Kirk Miller*

Abstract

Random thermal spikes have been experimentally observed at ambient temperature in small palladium metal foils electrolytically loaded with deuterium. We believe these spikes can be identified with deuterium fusion events triggered by alpha-particle emission from a small amount of depleted uranium melted into the foils.

© 2025 ICCF. All rights reserved. ISSN 2227-3123

Keywords:

1. Introduction

The objective of this research was to investigate the viability of a patent application of one of the authors, Douglas Pinnow, namely Patent Application Publication No. U.S. 2016/0314856 A1, dated 2016 October 27 and titled *SPONTANEOUS ALPHA PARTICLE EMITTING METAL ALLOYS AND METHOD FOR REACTION OF DEUTERIDES*. Our hypothesis is that a radioactive triggering event, either incidental or deliberate, is required to initiate a deuterium-fusion reaction in the palladium electrode of a Fleischmann and Pons-type electrolytic cell. The results of our experiments show that the spontaneous decay of an alpha particle-emitting isotope (such as uranium-238) in palladium metal loaded with deuterium will cause very brief and localized heating, which we calculate can raise the temperature at a microscopic scale in the immediate vicinity of the alpha-emitter to a value comparable to that found inside of the sun, enough to induce fusion of nearby deuterium ions. Such localized heating has long been known [23] but is not widely recognized. Since it is essential to the work covered in this paper, it is quantitatively explored in Appendix A. The heat generated by a deuterium-deuterium fusion reaction along one pathway, $D + D \rightarrow$ tritium + proton, produces 4.03 MeV of thermal energy, which may cause additional fusion events and potentially lead to a chain reaction. The patent application publication cited above proposes that this process may be a viable alternative energy source to fossil fuels.

*For a virtual tour of the laboratory, click [here](#).

In our experiments we have consistently observed temperature spikes on a macroscopic scale in an alloy of 99% palladium and 1% depleted uranium (principally uranium-238). The temperature spikes occur only after the foils have been loaded with deuterium ions by a rather conventional electrochemical process. This result is consistent with the results announced by Martin Fleischmann and Stanley Pons in a press conference held at the University of Utah on March 23, 1989. That conference was broadly covered on national TV and in the press [2]. Their work, dubbed ‘cold fusion’ by the press, became a cover story of *Time Magazine* in 1989 [3].

In short order, the story was heavily criticized and ultimately dismissed by most of the scientific community because it had not been reproduced by others with the consistency necessary to support such a world-changing claim [4]. (See Appendix F for our evaluation of two failed attempts to replicate their findings.) The major difference between the present work and that of Fleischmann and Pons is that they never contemplated the addition of alpha-particle emitters into their palladium cathode to help trigger (initiate) the fusion.

In stark contrast to many protracted attempts to reproduce Fleischmann and Pons’ work, which mostly ended in failure, we found that after approximately two hours of electrolytic loading with deuterium, our palladium electrode consistently produced temperature spikes that were detected by attached thermocouples. We attribute the promptness and consistency of our results to the addition of a small amount of depleted uranium to the foil (1% by mass), the spontaneous decay of which we believe provides sufficient energy to trigger deuterium fusion in the foil. Both deuterium and a spontaneous radiation source were required to achieve positive results. Temperature spikes were not observed in test runs where we used a palladium-uranium foil in an electrolyte made from normal water (H_2O), nor in runs with an electrolyte made from heavy water (D_2O) but using a palladium foil without uranium – which rules out the possibility that the observed temperature spikes were merely caused by alpha decay. We found the pattern of temperature spikes when both heavy water and a triggering source were used to be random over the surface of the foil as well as random in time. We calculated that the substantial magnitude of the spikes could not possibly be due to a single alpha-particle emission or a single deuterium-deuterium fusion reaction. Rather, billions of such reactions must have been involved, closely clustered in time as a chain-reaction (see Appendix C). Others have also suggested the possibility of chain reactions related to the Fleischmann-Pons effect, including the report of explosive equipment damage in one case [5] and enhanced neutron emissions in another [6].

Based on these results, we believe that we turned our palladium foils into miniature nuclear fusion reactors that reached criticality. We have found that their power output can be controlled by adjusting the electrolytic loading current much like the output of a conventional fission reactor is controlled by moving its control rods.

We identify our results with the broad topic of SOLID-STATE FUSION (SSF), in contrast to the PLASMA FUSION that presently dominates the field of fusion research. SSF is being broadly investigated around the world in government institutions, universities, and industrial companies [22], [8]–[10]. Yet heretofore SSF has not been broadly accepted as a legitimate science, and the basic physical principles behind it remain elusive. The present work represents a strong confirmation of SSF.

2. Description of the Experiment

Our experiment was designed around three basic approaches: (1) to take full advantage of the electrochemical methods reported by Fleischmann and Pons, and those who followed them, for loading palladium with deuterium; (2) to substitute a thin palladium foil, that could be loaded with deuterium relatively quickly, for the more massive cylindrical rod employed by Fleischmann and Pons; and (3) to calculate the degree of deuterium loading by precisely measuring the change in mass of the palladium foil.

Further discussion on these three approaches follows to help those who may wish to confirm our results or go beyond them:

(1) Fleischmann and Pons did not report their work in sufficient detail to easily evaluate it and their claims. A photograph of Fleischmann and Pons holding their electrochemical cell was shown on the cover of *Time Magazine* in 1989 [3]. Their cell consisted of a quart-sized glass dewar with a rod-shaped palladium cathode surrounded by

a concentric helical coil of platinum-wire anode. The palladium cathode was approximately 6 mm in diameter, and both the cathode and anode, as well as a thermometer, passed through a rubber stopper at the top of the dewar. The dewar was filled with an electrolytic solution of lithium ions in heavy water (D_2O). A battery connecting the palladium cathode and the platinum anode drove the electrolytic charging of the palladium with deuterium to some unreported level. While such a description served as a useful starting point, there were many parameters that needed to be filled in by later researchers who attempted to verify Fleischmann and Pons' work.

One significant unknown is the concentration of their electrolytic solution. Following previous researchers, we decided on a 10-weight-percent solution of lithium deuterioxide ($LiOD$) in heavy water (D_2O). Due to the high price and extremely long delivery time (over one year) required to acquire $LiOD$, we decided to make it ourselves by chemically reacting lithium metal with heavy water. (To see how we made this solution, click here.)

Another decision we made was to gradually increase the loading current, starting with a low 30 milliamperes for the first 20 minutes, increasing to 60 milliamperes for the next 20 minutes, followed by a further increase to 120 milliamperes. This schedule was chosen to mitigate the possibility of stress-related cracking of the palladium foil [11]. In some cases, further increases to 240 and 300 milliamperes were explored with the objective of loading the foil with a higher concentration of deuterium. We found that these higher currents tended to increase the magnitude and frequency of the temperature spikes we observed in the foils.

Importantly, we calculated (see Appendix B) and subsequently observed that the time required to load our 1.2-gram palladium foils with an electrical current of 120 milliamperes was approximately $2\frac{1}{2}$ hours. This was short enough to complete a deuterium-loading run and produce temperature spikes on the same day.

(2) As a practical matter, the price of palladium has substantially increased since Fleischmann and Pons conducted their research in 1989. It is now comparable to that of gold. We therefore chose to use modest-sized palladium cathodes to keep costs down for us and for others who might continue our research. Our choice for the shape of the palladium cathode was also an important decision. We decided on thin flat foils of palladium metal with the objective to reduce the time required to load the palladium with deuterium, as that time depends on the distance of diffusion into the metal. We selected palladium foil $125\ \mu\text{m}$ (nominal 0.005 inches) thick. We found that postage stamp-sized cathodes, cut to $2\text{-cm} \times 2\text{-cm}$ square, were convenient to handle, and we are confident that our results using them reflect the behavior of bulk palladium (see Appendix D) rather than the behavior of the thin films that have been used in other related research [12], [13].

Over the years, many attempts have been made to duplicate the positive results of heat production reported by Fleischmann and Pons in 1989. The main guiding principle for these efforts has been to set up electrochemical cells like that of Fleischmann and Pons and to wait with great patience for heat production to begin while loading the palladium electrode with deuterium. Some researchers charged their cells for days, weeks, and even months in hopes of success – all the while bubbling off expensive heavy water from their electrolyte. Many gave up in frustration. But Fleischmann and Pons encouraged patience, advising that cell-charging should continue for at least three months before abandoning a nonperforming cell. Subsequently, McKubre and Tanzella [14] drew the *empirical conjecture* that high Pd/D ratios and high current fluxes “must be maintained for hundreds of hours sufficient to produce a new state or phase which gives rise to an anomalous excess heat. . .”

Over the past four decades, a limited number of partial successes have been reported, but reproducibility has remained elusive and the results continue to be clouded in uncertainty and doubt, tainted by the fact that even Fleischmann and Pons were unable to consistently repeat the world-shaking results that they had reported in 1989.

Our work has been guided by a much different strategy than having patience. Quite the opposite. We discovered that if we could load a palladium foil that contained a small amount of well-dispersed uranium-238 with a sufficient concentration of deuterium, heat production on a macroscopic scale would quickly follow. We interpret this as localized fusion triggered by the high temperatures produced at a microscopic scale by the spontaneous alpha decay of the uranium. There is no need to stress patience or to speculate on the production of a new state or phase of matter.

(3) One of our objectives to facilitate this research was to precisely monitor the deuterium loading in the palladium foil so that we could determine when we had reached the critical deuterium concentration that would support a deuterium-deuterium fusion chain reaction [24]. It was our premise that a sufficiently high concentration of deuterium would be required to sustain such a reaction, just as a high concentration of uranium-235 is required to reach criticality in a conventional fission reactor. Pinnow, who worked at the U.S. Atomic Energy Commission in the 1960's, knew that an external triggering event, initiated by a source that produces neutrons, is helpful to begin a chain-reaction when a fission reactor first starts up operation. By analogy, his 2016 patent application publication, mentioned above, claimed that alpha-particle decay would be helpful to initiate a chain-reaction in a fusion reactor charged with deuterium. This research effort was initiated in part to support that patent application.

The technique we settled on to monitor the deuterium-loading level in the palladium was to employ a very sensitive scale to measure the change in weight of the foil. The scale, a Mettler Model XSR64, has a precision of one ten-thousandth of a gram. To the best of our knowledge, this is the first time such a sensitive instrument has been used in conjunction with fusion research.

While all metals are known to absorb a limited amount of hydrogen or deuterium, palladium is unrivaled in its capacity to absorb large amounts of deuterium in an electrolytic cell. We watched this process taking place in a transparent borosilicate glass cell 80 mm in diameter, with a capacity of 100 ml. This cylindrical shaped cell offered a 360-degree view of the electrolysis. It is worth mentioning here that we left the top of our cell open during the deuterium-loading runs. This provided extra visibility of the palladium foil and facilitated its quick removal for weighing. (In most cases, it is prudent during electrolysis to use a closed cell that is well ventilated to avoid possible explosions when the effluent oxygen and hydrogen gases are released. However, due to the small size of our test samples, the total amount of hydrogen (deuterium) gas generated during a charging run was very low, in the range of 0.01 grams. Adequate ventilation was accomplished simply by opening a nearby window.)

3. Sample Preparation

Our preparation procedure started with a one-gram sample of highly purified depleted uranium. We used a file with a fine pitch to file off approximately 5% of the uranium metal. This was done inside of a sealed glove box and we carefully monitored the radiation level with a hand-held Geiger counter. The filings were guided to fall onto the surface of a 2-cm × 4-cm foil of 99.9%-pure palladium [15]. This foil was then folded in half to make a 2-cm × 2-cm foil with the uranium sandwiched between two layers of palladium. The sandwich was then run through a small rolling mill to secure the filings in place.

Next, the sandwich was placed onto a refractory block of ceramic alumina and heated above the melting point of palladium (1,552 °C) and well above the melting point of uranium (1,132 °C) using a small oxy-hydrogen torch. Uranium is miscible in palladium.

During heating, the palladium melted and surface tension caused it to form into a smooth button shape that was smaller and thicker than the original foil. We turned this button over and continued heating for several additional minutes with the objective of providing time for the uranium to disperse into the melted palladium matrix. After cooling, the palladium/uranium bead was rolled back into a foil in the rolling mill, using many small thickness-reduction steps to reduce the possibility of fracture. This rolling process took approximately one hour. (Sample preparation can be viewed by [clicking here](#)).

4. Setup

The center of the experiment was a simple electrolytic cell. This consisted of an open borosilicate dish filled with a concentrated electrolyte, a 10 weight-percent solution of LiOD in D₂O. For the cathode, we submerged the palladium-uranium alloy foil fully into the electrolyte and attached it to an insulated platinum wire that connected it to the power

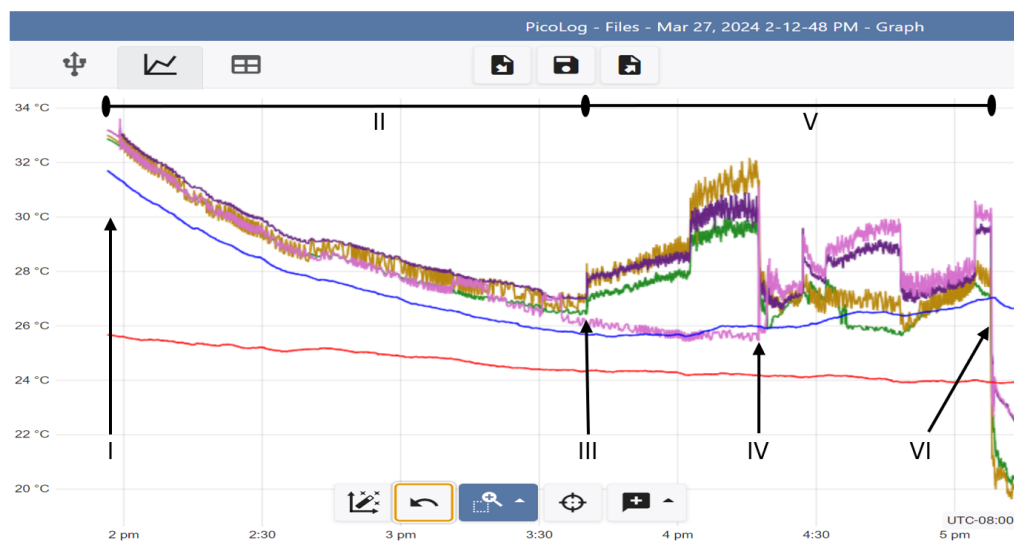


Figure 1. Compressed view of the entire deuterium-loading run. Note the changing lab temperature (red trace) and electrolyte temperature (blue trace). The green, violet, ocher and pink traces are the four thermocouples. The main events in this figure are indicated by Roman numerals: (I) Start of run. (II) Region of sub-critical electrical charging of the palladium foil. (III) First temperature spikes (shown in expanded detail in Figs. 2) as regions of the palladium cathode go critical and heat production starts at three of the thermocouples; the temperature of the electrolyte drops gradually toward ambient air temperature in (II), but after (III) starts rising again. (IV) Moment when the fourth channel goes critical, as signaled by the large temperature spike and subsequent drop in temperature in all channels, as shown in detail in Fig. 3. (V) Region of critical operation of the palladium foil fusion reactor. (VI) End of the run. The loading current was increased at (III), again between (III) and (IV) just after 4 pm, and again at (IV). Between (IV) and (VI) there was a temporary reduction in charging current and a corresponding reduction in power output due to a problem with a wiring connection. The problem was corrected before the end of the run.

source. For the anode we used a plain platinum wire. K-type (nickel-alumel) thermocouples were clamped to the palladium foil; the more thermocouples were used, the more temperature spikes were detected. For the run illustrated in the figures, four thermocouples were used, attached with a pair of spring-loaded clips spaced approximately 1 cm apart. One thermocouple under each clip was in contact with the front surface of the foil, the other directly behind it on the back surface. Leads from the thermocouples were run through a multi-channel data logger (Pico Technology USB TC-08). The locations of these thermocouples on the foil, and the corresponding numbers of the data-logger channels and colors of the traces of each channel in the figures are as follows:

- Left front: Channel 3 (Green),
- Left back: Channel 4 (Ocher),
- Right front: Channel 5 (Pink),
- Right back: Channel 6 (Violet).

We used two additional thermocouples to measure the ambient temperature of the cell and of the palladium foil:

- Channel 1 (Red) Air temperature in the lab
- Channel 2 (Blue) Electrolyte temperature in the cell

The list of channels is displayed in Fig. 2B.

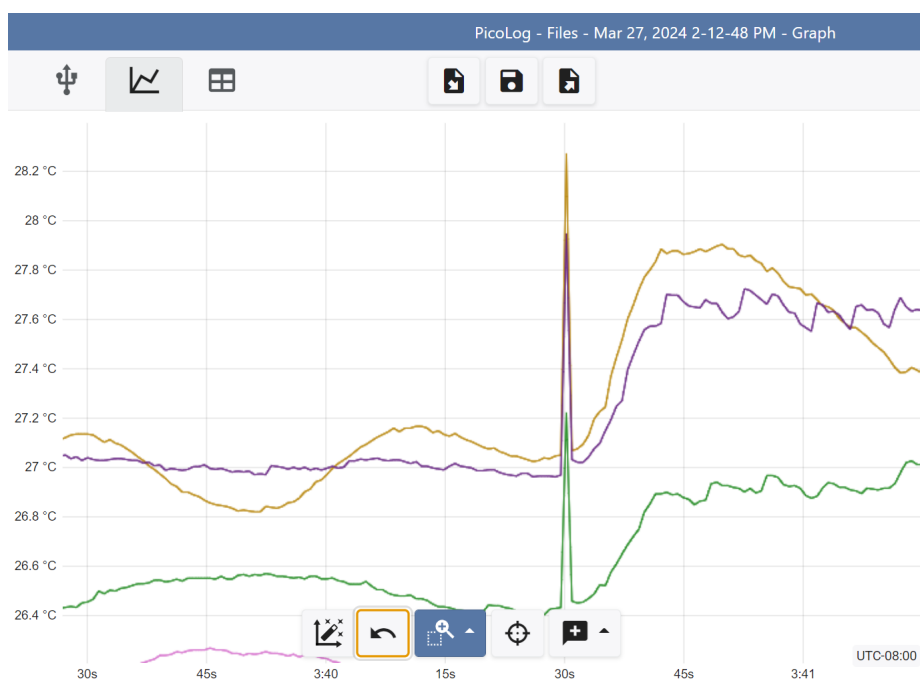


Figure 2A. Simultaneous temperature spikes on three thermocouples at 1 hour and 43 minutes after starting the deuterium-loading run. This event is marked (III) in Fig. 1.

5. Results

We started our first deuterium-loading run using a palladium-uranium foil with only a single thermocouple attached. We began with an electrolytic charging current of 30 mA. No gas bubbled off the palladium foil, indicating that the deuterium produced by the electrolysis was being fully absorbed. We increased the current to 60 mA half an hour in, and to 120 mA at 45 minutes. At 2 hours 14 minutes into the run – approaching the time we calculated it would take to fully load the palladium with deuterium (see Appendix B) we saw what appeared to be a temperature spike of 1.2 °C. By the end of the four-hour run we observed three more apparent temperature spikes.

The following table shows the times after the start of the run that the four apparent temperature spikes occurred, their peak changes in temperature and the loading current at the time of each spike:

Spike Number	Time after Start	Loading Current	Delta Temp.
1	2 hr, 15 min	180 mA	+1.1 °C
2	3 hr, 18 min	240 mA	+0.2 °C
3	3 hr, 23 min	240 mA	+0.2 °C
4	3 hr, 24 min	240 mA	+0.1 °C

All of the spikes returned to baseline temperature within 1 second.

After observing these apparent temperature spikes, we decided to halt the run to investigate their cause. Initially, we were unsure if they were due to fusion events or were simply glitches caused by some defect in our monitoring equipment. We eventually ruled out the latter by making several subsequent deuterium-loading runs that consistently

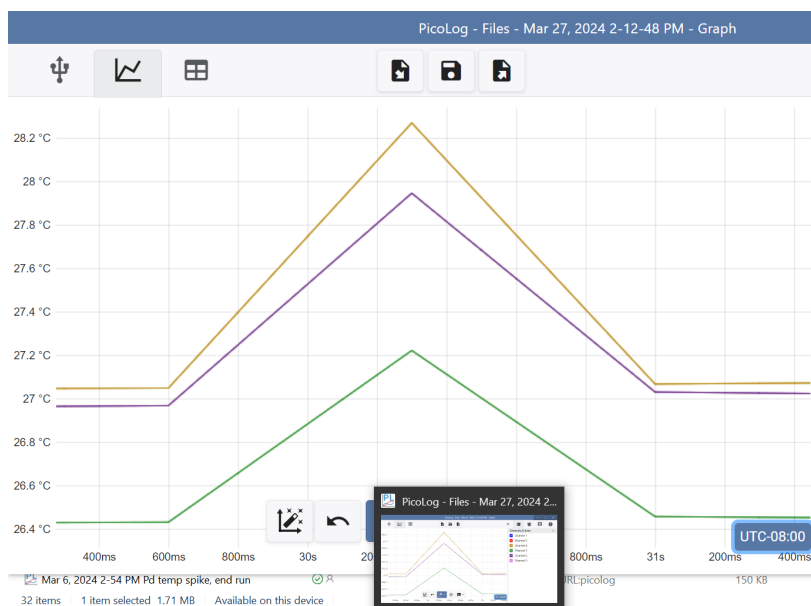


Figure 2B. Expanded scale of the event seen in Fig. 2A. The three spikes are simultaneous to within the measurement resolution of our equipment: Their widths are limited to 1/10 second by the response time of the low-mass thermocouples that were used.

produced multiple temperature spikes with similar time signatures. For these runs we decided to use a total of four fast-responding thermocouples (one tenth-second response time) so that we could better observe the temporal and spatial distribution of the temperature spikes over the surface of the foil. We also refreshed our electrolyte solution to eliminate the possibility of cross-contamination from earlier charging runs.

During our final run using a palladium-uranium foil with these equipment changes (Fig. 1), we observed multiple temperature spikes, shown in Fig. 2, 3, and 4. How exciting it was to see the multitude of random temperature spikes recorded in Fig. 4!

The traces in Fig. 2A show that three of the four thermocouples (Channels 3, 4, and 6) recorded reaching criticality simultaneously, with temperature spikes of 0.8 °C, 1.0 °C and 1.2 °C, respectively. The fourth thermocouple (Channel 5) remained unaffected. Fig. 2B shows the same event with an expanded time scale. One can see that the temperature spikes occurred at the same time in all three active channels. This implies that wherever the fusion event was first triggered in the palladium foil, it propagated so fast that we could not resolve its advance. This indicates a propagation speed greater than 10 cm per second, as the thermocouples on Channels 3 and 6 were placed approximately 1 cm apart and our minimum sampling-time interval was 0.1 sec. One gets a picture of a macroscopic deuterium fusion event that quickly filled the space between thermocouples 3, 4, and 6 and then, almost as quickly, died out – likely due to depleting the deuterium that had been maintaining criticality in this region. During the following 10 seconds, the temperature built up at thermocouples 3, 4, and 6 and more temperature-spiking continued at a somewhat lower level and persisted long after.

As the electrolytic charging of the foil continued, it is reasonable to assume that the concentration of unreacted deuterium near the quiescent thermocouple 5 continued to increase until it also ‘fired off’ 38 minutes later with the largest temperature spike that we observed (5.7 °C). This extraordinary temperature spike is shown in Fig. 3. It should also be noted in this figure that there were simultaneous temperature reductions in thermocouple channels 3, 4, and

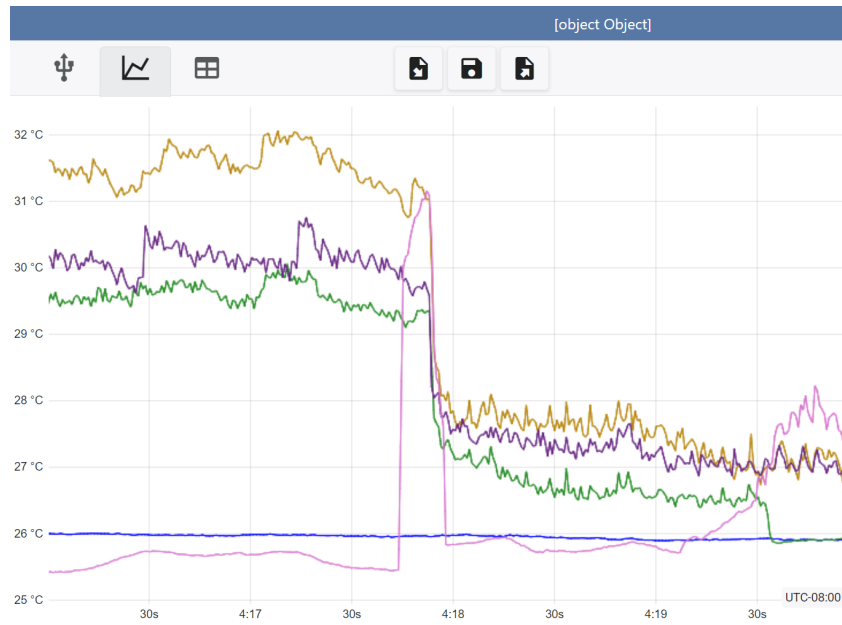


Figure 3. The largest temperature spike observed, at 5.7 °C (pink). This event is marked (IV) in Fig. 1. It was followed by immediate temperature drops on all channels. These drops were unexpected but are now believed to be understood, as discussed in the text.

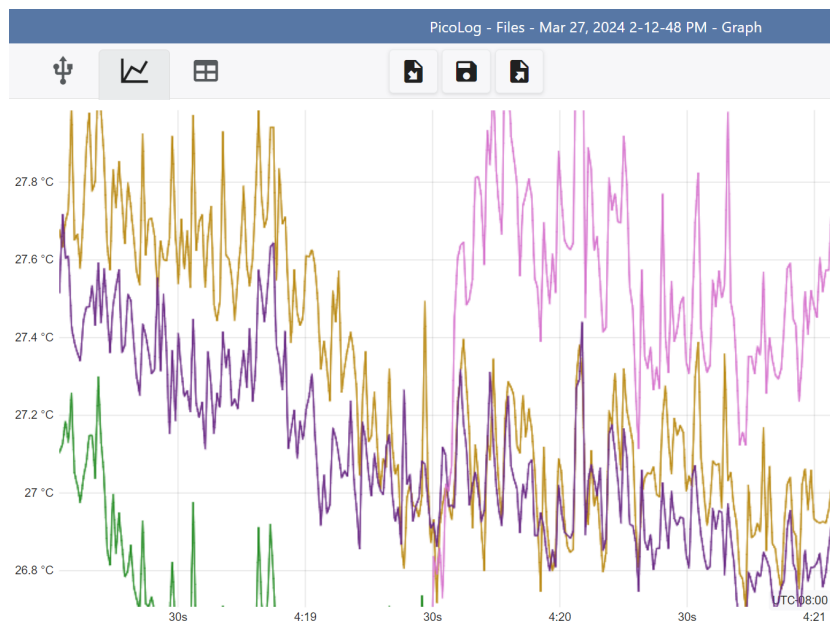


Figure 4. Numerous temperature spikes observed after reaching criticality. The time starts 30 seconds after the large spike seen in Fig. 3, with an expanded vertical scale.

6. At first, we were puzzled by these unexpected temperature reductions. Eventually we realized that the very large temperature spike in the region of thermocouple 5 may have reduced (burned out) quite a lot of deuterium in this location and this may, in turn, have caused deuterium ions in regions 3, 4, and 6 to quickly move to fill the void in region 5. On the short term, this would tend to reduce power production in regions 3, 4, and 6, as observed, followed by a return to temperature-spiking in these regions, but at a somewhat lower level than before the 5.7 °C temperature spike in region 5. Subsequent temperature-spiking at a reduced level continued in all four thermocouple channels until the end of the deuterium-loading run.

Fig. 1 provides a compressed overview of the data we collected during this electrolysis run. There one can see that the thermocouple monitoring the ambient air temperature in our laboratory (Red) showed a slow but monotonic decline as the afternoon sun was setting, and that the thermocouple monitoring the temperature of the electrolytic bath (Blue) began showing a slow increase after the temperature spikes began (region V on the plot). By the end of the run, the temperature of the electrolytic bath had increased by approximately 1.5 °C relative to the minimum value measured at the first temperature spike, while the ambient air temperature continued to decrease. While some of this increase relative to the electrolyte bath might be attributed to electrical heating associated with electrolysis, we saw no such effect in an immediately prior run using a palladium foil that did not contain any added uranium. We concluded that most of the temperature increase was caused by nuclear fusion.

6. Conclusion

After considering many improbable alternatives, we believe that the extensive thermal spiking we observed confirms Solid State Fusion. The substantial magnitude of the spikes seen in the figures could not be due to single alpha-particle emissions or to single deuterium-deuterium fusion events. Rather, many reactions must have been clustered closely together in time. Specifically, we calculate in Appendix C that 3×10^9 fusion events would be required to produce enough energy to raise the temperature of our thermocouple by 1 °C.

We find it helpful to think of the palladium foil in its electrolytic cell as analogous to a conventional fission-reactor core inside its reactor vessel, and believe that the temperature spikes we observed were due to transient nuclear-fusion chain reactions triggered by alpha decay of the uranium mixed into the foil, similar to what happens during the cold startup of a fission reactor when control rods are pulled and a chain reaction begins. If this is the case, the fact that the power output is in the form of spikes, rather than sustained at a continuous level, suggests that the palladium foil must have been operating just above the critical level. As calculated in Appendix C, each alpha-decay triggering event would have to be multiplied by a factor of at least 3×10^9 .

We calculate that an alpha decay produces extraordinarily high, albeit extremely localized, temperatures within the palladium crystal lattice (see Appendix A), temperatures sufficient to initiate a fusion chain reaction among the deuterium ions dispersed in the lattice. This means that ‘cold fusion’ is not actually a cold process. Rather, ‘cold fusion’ is a misnomer for a process better defined as ‘solid-state fusion,’ which occurs at temperatures comparable to those inside the sun.

This explanation goes a long way to account for the mysteries surrounding Fleischmann and Pons’s inconsistent results, as well as the many frustrating attempts to replicate them. The likely explanation for some previously claimed successes in achieving ‘cold fusion’ by very patient researchers who waited weeks and months for heat production to begin, is that these results were likely due to fortuitous fusion reactions triggered either by a random cosmic ray or by the spontaneous decay of a trace radioactive contaminant in their palladium. Other researchers were not so lucky. Appendix F describes two major projects that were started in 1990s to replicate the work of Fleischmann and Pons, and why they may have failed.

Try to think of the possibilities for a solid-state fusion reactor the size of a postage-stamp!

7. Acknowledgements

The authors are particularly grateful to Dr. Frank Dabby, Chairman of ASI Silica Machinery, who generously provided the primary funding for this this research effort, and to Wendy Amberg and Robert Otero as well as the other staff members at ASI Silica Machinery, who procured most of the equipment that was used and helped to set it up. The authors also wish to thank Lynn Bowen, Adjunct Professor at Colorado Mountain College, who provided important advice and guidance before and during this project.

APPENDIX A: Temperature of an Alpha-Particle Decay

When any atom undergoes a nuclear reaction, fission or fusion, in a solid material, nuclear energy is released in the form of rapidly moving subatomic byproducts that can impact neighboring atoms so vigorously that localized melting, quickly followed by refreezing, occurs on a microscopic scale. This effect is known to cause a substantial increase in the total number of atomic voids in metals [23]. This discovery was made by researchers who were recruited in the 1940s to 1960s to direct programs that would investigate the cumulative effects of radiation on the materials used to build nuclear fission reactors. One of their most significant findings is that metals tend to swell (typically by 2% to 5%) and distort under continual neutron bombardment, due to the accumulation, over the lifetime of a typical nuclear reactor, of these atomic voids.

The focus of these researchers was on the mechanical strength and durability of materials under irradiation, not on the local temperatures that occurred during these events. If one asked a mainstream physicist how high the temperature goes within such a submicroscopic burst of heat produced by a fission or fusion event, they would likely be reluctant to give a definitive answer because temperature is defined by the average kinetic energy of a group of particles in thermodynamic equilibrium. The physicist would tell you that the atoms involved in such submicroscopic bursts heat up and cool down so quickly that there is not sufficient time to establish thermodynamic equilibrium. But if pressed, the physicist would likely agree with Wigner and Seitz that shortly after the peak of the burst the total released nuclear energy would be shared by, say, ten thousand or so neighboring atoms [23]. Since the fusion of two deuterium atoms releases 4.03 million electron volts (MeV) of energy, each atom within such a burst region would on average acquire roughly 403 electron volts of thermal energy. As the kinetic energy is proportional to temperature, and the average thermal kinetic energy of an atom at room temperature ($20\text{ }^{\circ}\text{C} = 293\text{ K}$) is $1/40\text{ eV}$, one can very approximately estimate the temperature in the neighborhood of a nuclear event to be $T = (403\text{ eV})(293\text{ K})/(1/40\text{ eV}) = 4.7\text{ million kelvin}$. Such a high temperature is typical of most spontaneous nuclear reactions, both fission and fusion. The kinetic energy would be much higher for atoms that are closer to the fission or fusion event, likely approaching or exceeding the energies associated with the 15 million-K temperature in the fusing core of the sun.

APPENDIX B: Foil-Charging Time

Many researchers who have attempted to reproduce Fleischmann and Pons' 1989 results believe it is essential to load the palladium with an extremely high concentration of deuterium for heat to be produced. Michael McKubre, a former student of Fleischmann's and subsequently Director of the Energy Research Center at the Stanford Research Institute (SRI International) in Palo Alto, California (now retired), reported that the ratio of deuterium ions to palladium atoms should be 0.875 or greater – that is, a ratio of $\text{PdD}_{0.875}$ or greater [24]. To reach this level requires high-quality palladium and considerable care in loading.

Although some researchers observed excess heat-generation only after days or weeks of electrolysis, the deuterium-loading time should not be nearly that long. Faraday's Law of Electrolysis can be used for a rough estimate. The following calculation finds the minimum time to achieve a deuterium/palladium ratio of 1.0, in the ideal case that all deuterium dissociated at the palladium cathode is absorbed by it.

One can estimate the time, t , to load a palladium cathode with deuterium by equating the electrical charge, Q , delivered by a current, I , to produce a number of deuterium ions equal to the number of palladium atoms in the cathode, in a 1:1 ratio. Specifically:

$$Q = I \times t = \text{number of palladium atoms in the cathode} \times \text{charge per deuteron} \\ = (\text{moles of palladium, } n)(\text{Avogadro's number, } N_A)(\text{electron charge, } e)$$

Solving for t results in:

$$t = nN_A e / I = nF / I \quad (1)$$

where $F = N_A e$ is the Faraday constant and $t = nF / I$ is Faraday's second law [17].

Setting these to the mass of our cathode and a moderate current,

$$n = (1.2 \text{ g of Pd}) / (106.4 \text{ g/mole}) = 1.13 \times 10^{-2} \text{ moles} \\ F = 9.05 \times 10^4 \text{ Amp-sec/mole} \\ I = 0.120 \text{ Amp,}$$

results in a time of 2.5 hours (2 hours per gram of palladium) for full deuterium-loading of our cathode using our default loading current of 120 mA under ideal conditions. This result is in the range of the time we needed to run the electrolytic cell before observing temperature spikes in the palladium-uranium foil.

APPENDIX C: Number of Fusion Events Required for a Moderate Temperature Spike

The number of fusion events required to produce a temperature spike of 1°C can be approximated by equating the thermal energy necessary to heat the mass of the thermocouple tip by 1°C to the number of 4.03-MeV fusion events required to produce the same amount of energy. This assumes that the region of heating is in direct contact with the thermocouple and that all heat produced is transferred to the thermocouple, and as such is a lower bound.

The fast-responding nickel-alumel thermocouples that we used had a spherical tip of diameter $D = 0.9 \text{ mm}$, for a volume of $V = \pi D^3 / 6 = 3.8 \times 10^{-5} \text{ cm}^3$. The heat capacity, HC , for this bead can be calculated from the density, ρ (8.60 g/cm^3), and specific heat, SH ($0.125 \text{ cal/g}\cdot^\circ\text{C}$), of nickel-alumel [18].

$$HC = V \times \rho \times SH \\ HC \text{ (in MeV)} \\ = (3.8 \times 10^{-5} \text{ cm}^3)(8.60 \text{ g/cm}^3)(0.125 \text{ cal/g}\cdot^\circ\text{C})(4.184 \text{ J/cal})(6.2 \times 10^{12} \text{ MeV/J}) \\ = 1.06 \times 10^{10} \text{ MeV}/^\circ\text{C}.$$

Since each deuterium-deuterium fusion event produces 4.03 MeV of energy, a total of $(1.06 \times 10^{10} \text{ MeV}/^\circ\text{C}) / (4.03 \text{ MeV/event}) = 2.6 \times 10^9$ deuterium-fusing events are required to heat the thermocouple tip by 1°C . Based on the half life of uranium-238 relative to alpha particle decay of 4.468×10^9 years, we expect 200 alpha decays per second from the 18 mg of uranium in the foil.

APPENDIX D: Palladium Foil Behaves as Bulk Material

Palladium foil $125 \mu\text{m}$ thick behaves as bulk metal rather than as a thin film (such as those employed by Gordon *et al.* [12], [13]) because it requires approximately 32,000 palladium atoms to span the $125 \mu\text{m}$ thickness of the foil ($125 \mu\text{m} / 3.89 \text{ angstroms}$ between palladium atoms in their close-packed cubic lattice [22] = 32,000 atoms).

APPENDIX E: Pre-Polarized Oppenheimer-Phillips Effect

Early critics of Fleischmann and Pons' 1989 work on 'cold fusion' were quick to point out that the fusion reaction $D + D \rightarrow {}^4\text{He}$ produces the helium in an excited state that quickly decays with equal probabilities along two pathways (branches):

- (1) tritium + proton (${}^3\text{H} + p$), and
- (2) helium-3 + neutron (${}^3\text{He} + n$).

These critics predicted that the neutrons produced by the second branch would have been lethal to Fleischmann and Pons if they had actually observed fusion. However, there may be situations in which the second branch is not comparable in strength to the first. One possibility is related to the Oppenheimer-Phillips effect, which was first investigated by Robert Oppenheimer and Melba Phillips in 1935 [19], though critics have claimed that this effect is too small to explain the lack of irradiation [20]. Based on the considerable amount of experimental evidence accumulated since 1989, it would seem that the deadly neutron-producing branch is not significant inside of metals such as palladium. But why? One possibility that may be viable is a low-temperature variant of the Oppenheimer-Phillips effect. Since this possibility is preliminary yet potentially significant, it is introduced here in an appendix rather than in the text. (Several other fusion alternatives have been explored; one that was proposed by Edmund Storms, a reaction of $D + e + D \rightarrow {}^4\text{H} \rightarrow {}^4\text{He} + e + \text{neutrino}$, is also consistent with the survival of Fleischmann and Pons [21].)

We believe that a modification of the Oppenheimer-Phillips Effect can explain the lack of lethal neutron radiation generated by Solid-State Fusion.

By way of background, here is a description of the Oppenheimer-Phillips effect given by Robert B. Leighton [19]:

There are a few special situations which deserve special attention. One of these is that (deuteron, proton) reactions are much more commonly observed than would be expected . . . The reason for this was deduced by Oppenheimer and Phillips (1935). When a deuteron approaches a nucleus, the repulsion between the nucleus and the proton causes the deuteron to become polarized with its proton end farther from the nucleus. The proton-neutron bond distance for the neutron is of such a size (approximately 5×10^{-15} m) that the neutron can be inside the nucleus before the proton has surmounted the Coulomb barrier. The weak bond (2 MeV) of the deuteron is easily broken, so that the proton can be ejected and the neutron retained.

Applying this effect to two deuterons on a collision course that might lead to a fusion event, one would expect that the more likely outcome would be the formation of tritium + proton rather than ${}^3\text{He} + \text{neutron}$. However, Koonin and Mukerjee argue that there is insufficient time in a hot-fusion reactor for the incident deuterons to rotate into a polarized orientation before they collide [20]. This would mean that the Oppenheimer-Phillips effect should be small to negligible.

While this does appear to be the case in a hot fusion plasma, the situation may be entirely different under the conditions inside the solid-state palladium lattice. It is possible that under normal room-temperature conditions, the deuterium ions dispersed in palladium may rotate to a polarized orientation, and thus no additional time would be required for polarization when an alpha-particle emission or other triggering event occurs, even with the high transient temperatures estimated in Appendix A for such an event. In effect, the deuterium ions may exist as pre-polarized pairs in the PdD lattice – much as they do in molecular deuterium gas (D_2) – so that the reaction branch $D + D \rightarrow \text{tritium} + \text{proton}$ is favored over the production of neutrons. Under such conditions, the Oppenheimer-Phillips effect would dominate.

We realized that this pre-polarization in palladium metal may be a possibility after recognizing the high mobility of deuterium across the foil. The deuterium ions appear to move through the palladium lattice almost like a gas, as demonstrated by Fig. 3. Analogy to polarized di-atomic gas gave rise to the idea of pre-polarized deuterium ions in the

palladium host. X-ray and neutron-diffraction studies show that the hydrogen ions in palladium hydride occupy the center of the metal's face-centered cubic lattice structure [22]; palladium deuteride should be similar. Measurements of the magnetic properties of palladium hydride indicate that when the hydrogen concentration passes 62% of the palladium atom concentration, PdH_{0.62}, the material becomes diamagnetic [25]. This suggests anti-parallel spin alignment of nearest neighboring palladium ions at the higher concentrations required for fusion. If the magnetic moments of adjacent deuterium ions tend to align by spin-spin coupling, one would expect a substantially enhanced Oppenheimer-Phillips effect: When a localized compression wave from an alpha decay or other energetic event propagates through the lattice, the half of adjacent deuterium ions that are oriented so that the neutrons are closest will selectively react, favoring the D + D → tritium + proton pathway, while the half oriented so that the protons are closest will resist approaching one another, damping the helium-3 + neutron pathway. The net result is strongly biased towards the first pathway. We have chosen to name this behavior in palladium hydride the *Pre-polarized Oppenheimer-Phillips effect*.

APPENDIX F: Case Histories of Cold Fusion Failures

Two case studies are particularly worth mentioning because they highlight the need for a triggering source.

When Fleischmann and Pons had difficulty reproducing their cold fusion experiments in 1990, their institution, the University of Utah, decided to establish a substantial new facility, named the National Cold Fusion Institute (NCFI), to carry out cold fusion research on a scale beyond what had been possible in their chemistry lab. Initial funding for the institute was five million dollars. A seasoned scientific manager with considerable industrial experience was hired to direct the Institute's efforts. Early on in this assignment, he decided to eliminate as many experimental variables as practical. Critically, he decided to use very high-purity palladium to eliminate the possibility that some unknown contaminant might influence the results. Eventually more than one hundred experiments were conducted, and all failed to produce any substantial excess heat – the work of the Institute was a total failure. When funding ran out in 1991, the institute was shut down, the director lost his job, and the careers of Fleischmann and Pons were destroyed. No one at the time had any idea of what had gone wrong. (Note: While the NCFI did not report any positive replication of Fleischmann and Pons' results, they *did* report positive results for tritium production [27] and observation of minor bursts of excess heat bursts [28].)

Considerably later, Pinnow had an opportunity to review many of the results at the Institute and elsewhere. He realized that the decision to use high-purity palladium was likely a fatal mistake. That decision eliminated the use of radio-frequency induction furnaces for the purification of the palladium that they used. It turns out that thorium (an alpha-particle emitter) is a typical trace contaminant in materials processed in these furnaces, which are used in many laboratories [26]. A low-density thorium oxide material, called *thorium frit*, is often used for support structures inside these furnaces. Some spalling of this frit occurs when the furnace temperature reaches high temperatures such as the melting point of palladium (1552 °C) [26]. It is necessary to exceed this temperature so that heavy impurities in the palladium will sink to the bottom of the melt and lighter impurities will float to the top, where they can be removed. The spalling at such temperatures can cause minor thorium-oxide contamination of the material being processed. Without some radioactive contamination of this nature in the palladium electrode to serve as a trigger for deuterium fusion, the experiments at the Institute were likely doomed.

There is another instance where the use of very high purity palladium did not produce hoped-for results: A program sponsored by the Japanese Ministry of International Trade and Industry (MITI) in the 1990s supported attempts to replicate the Stanford Research Institute's (SRI) version of the Fleischmann-Pons experiment, but with 0.99999-pure palladium in an effort to eliminate sources of inconsistency, including background contamination, between experiments conducted at different laboratories. Several hundred experiments were done around the world under this initiative. At the end, no one had positive results to show for years' worth of effort. This further supports our position that very high

purity palladium may not contain a sufficient content of nuclides capable of spontaneous alpha-particle decay and thus serving as fusion-triggering sources.

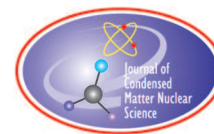
APPENDIX G: Hazard Analysis

Anyone undertaking experimental work in solid-state fusion is encouraged to conduct a diligent hazard analysis before proceeding. The consequences are potentially serious [5]. Our analysis revealed that if even a one-gram, postage-stamp-sized palladium foil were fully loaded with deuterium, and a single fusion chain-reaction were to somehow consume all of that deuterium, the resulting explosive release of energy would be in excess of 100 sticks of dynamite!

References

- [1] See “Effects of Radiation in Solids” by Nobel Prize winner Eugene Wigner and Fredric Seitz in Scientific American’s Commemorative Edition SCANOBELS15.
- [2] Reports covering the Fleischmann and Pons press conference on March 23, 1989, were broadcast that evening on the McNeil/Leher News Hour and covered by Dan Rather of the CBS Evening News. The next day, March 24, 1989, The Wall Street Journal made ‘cold fusion’ a top story in its worldwide news column.
- [3] *Time Magazine*, May 8, 1989.
- [4] John R. Huizenga, *Cold Fusion: The Scientific Fiasco of the Century*. Oxford University Press, 1993.
- [5] J.-P. Birberianm, Unexplained Explosion During Electrolysis Experiment in an Open Cell Mass Flow Calorimeter. *J. Condensed Matter Nucl. Sci.* 2 (2009) 1–6.
- [6] M. Buxerolle & J. Kurkdjian, An Historical Experiment of Neutron Detection Near an Electrolytic Cell. *J. Condensed Matter Nucl. Sci.* 21 (2016) 7–12.
- [7] Search on Internet, Solid State Fusion, Overview.
- [8] Pamela Ann Boss & Lawrence Forsley, A Synopsis of Nuclear Reactions in Condensed Matter. GEC Technical Report (2019).
- [9] L. Forsley, A Synopsis of Nuclear Reactions in Condensed Matter. GEC Technical Report (2019). doi.org/10.13140/RG.2.2.21903.23204.
- [10] David Nagel & Kamron Fazel, Low Energy Nuclear Reactions: Exciting New Science and Potential Clean Energy. *Fusion Science and Technology*, volume 61, pp. 463–468 (2012, published online 2017).
- [11] Dennis Cravens, Factors Affecting the Success Rate of Heat Generation in CF Cells, 4th International Conference of Cold Fusion. ICCF 4 Paper 18, 1993.
- [12] S. Szpak, P.A. Mosier-Boss, et al. Technical Report 1862, US. Space and Naval Warfare Systems Center in China Lake, California, 2002.
- [13] Frank Gordon, CF/LENR Colloquium 2014. Codeposition Protocols for Preparing Cold Fusion Cathodes, YouTube.com/watch?v=wlkqtloesji. See minutes 5:13 to 6:03, which show flickers of light corresponding to fusion events in thin films.
- [14] M.C.H. McKubre & F.L. Tanzella, Materials Issues of Loading Deuterium into Palladium and the Association with Excess Heat Production. In *The Seventh International Conference on Cold Fusion*, April 1998.
- [15] Surepure Chemetals, L.L.C. Florham Park, New Jersey.
- [16] Michael McKubre: youtube.com/watch?v=VnUOMg7MkoQ and “60 MINUTES – COLD FUSION IS HOT AGAIN.” (Covers important work by McKubre at the Stanford Research Institute.) Runtime 12:52 minutes.
- [17] See Wikipedia article “Faraday’s law of electrolytes,” where Equation (1) is more fully discussed.
- [18] Physical Properties of Thermolement Materials: Thermolement Material. Omega.com.
- [19] Robert B. Leighton, *Principles of Modern Physics*. McGraw-Hill Book Co., 1959, p. 587–588.
- [20] Koonin & Mukerjee, Branching ratios in low-energy deuterium-induced reactions, *Phys. Rev.* C42 1639, 1990.
- [21] Edmund Storms, The Nature of Cold Fusion (Cold Fusion Made Simple), *Condensed Matter Nucl. Sci.* 38, 2023, p. 130–146.
- [22] WebElements: Palladium – $_{46}\text{Pd}$: crystal structures. webelements.com/palladium/crystal_structure.html
- [23] See Wikipedia article “Faraday’s law of electrolytes,” where Equation (1) is more fully discussed.
- [24] Manchester, F. D.; San-Martin, A.; Pitre, J. M. The H-Pd (hydrogen-palladium) System. *Journal of Phase Equilibria*. **15** (1): 62–83. February 1994. doi: 10.1007/BF02667685. S2CID 95343702.

- [25] Tatsuya Kawae, Yuji Inagaki, Si Wen, Souhei Hirota, Daiki Itou & Takashi Kimura. Superconductivity in Palladium Hydride Systems. *Journal of the Physical Society of Japan*. **89** (5): 051004. 15 May, 2020.
- [26] Private communication, L. G. VanUitert, Bell Labs, Murray Hill, NJ (1972).
- [27] F.G. Will, K. Cedzynska & D.C. Linton, Reproducible tritium generation in electrochemical cells employing palladium cathodes with high deuterium loading. *Journal of Electroanalytical Chemistry*, 360(1-2), pp. 161–176, 1993.
- [28] F.G. Will, K. Cedzynska, M.C. Yang, J.R. Peterson, H.E. Bergeson, S.C. Barrowes, W.J. West, & D.C. Linton, Studies of electrolytic and gas phase loading of palladium with deuterium. In: *The Science of Cold Fusion, Proc. II Annual Conf. on Cold Fusion, Como (Italy)*. June 1991.



Research Article

Thermodynamics in Lattice Assisted Nuclear Reactions

Mitchell R. Swartz, ScD, EE, MD

JET Energy, Inc., Wellesley, MA USA

Abstract

Thermodynamics studies energy and is requisite to better understand the pathway to more reproducible cold fusion (LANR) systems with higher incremental power gain. As a theoretical model, it has a few problems but they are very well defined.

© 2025 ICCF. All rights reserved. ISSN 2227-3123

Keywords: Zeroth Law, First Law, Second Law, Third Law, Calorimetry, Navier-Stokes, Bremsstrahlung, entropy

1.1 Introduction - Key to understanding Physical and LANR systems

Thermodynamics is the study of the relationships and conversions between heat and several types of energy: mechanical, electrical, radiant, nuclear, and chemical [1,2,3]. It is critical to understanding physical systems including lattice assisted nuclear reactions (LANR) systems. It also impacts and is the key to better understanding electrodes, diagnostics, and emissions.

Etymology - The word root ‘thermo’ derives from the ancient Greek word $\theta\acute{\epsilon}\rho\mu\eta$ (pronounced ‘therme’) which means heat, and $\theta\epsilon\rho\mu\acute{o}\varsigma$ (pronounced ‘thermos’) means hot, glowing, and boiling. The word root ‘dynamics’ shares use with dynamite and dynamo and dynamic [4]. “Dyne” comes from the Greek word $\delta\acute{\upsilon}\nu\alpha\mu\iota\varsigma$ which means ‘power’ and was derived from the Greek translation of “koach” [קֹחַ], the Hebrew word used in the Bible to describe the miraculous deliverance of Israel at the Sea of Reeds [Exodus 15.6]. The word ‘energy’, itself, comes from ancient Greek: $\acute{\epsilon}\nu\acute{\epsilon}\rho\gamma\epsilon\iota\alpha$ (pronounced ‘energeia’) which means activity or a moving, working system. The word was used in Aristotle’s writings, 2351 years ago. Aristotle wrote of two outcomes when dealing with energy:

“there is some difference between ends: some ends are energeia [energy], while others are products which are additional to the energeia.”

1.2 Problems of Thermodynamics

However, there are several problems with thermodynamics. The first one is that the actual origin of, and applications for, thermodynamics arise from observations and real complex systems involving matter and energy, and the analyses are really only close approximations. As discussed below, the second problem is that some of the “Laws” are not really Laws after all. Some are sometimes not even true, and one (the Third) is disproven by aqueous cold fusion (LANR)

systems. On the other hand, the first and second Thermodynamic Laws are linked fully both to our LANR systems and to all our measurements of their properties. In fact, from the measurements alone, thermodynamics is absolutely necessary, relevant, and critical for accurate energy accounting in experiments.

The bottom line is that one can better understand the scope, origin and applications of CF/LANR systems using these thermodynamic teachings. Therefore, the following review will discuss some of the origins and, most importantly, limitations.

2.1 Zeroth Law of Thermo - Required for “Temperature equilibration”

The Zeroth law of thermodynamics has been recently added to introduce the concept and property of matter known as “temperature equilibration”, which is needed for the subsequent Laws. It simply states that at equilibrium, two objects touching will eventually achieve the same temperature.

3.1 First Law of Thermodynamics - Conservation of Energy

The first law of thermodynamics involves both the conservation of energy theorem and the requisite need to consider energy balance. The First Law’s Origin begins with observations which were made by a physician looking at biological systems, then by an engineer trying to improve steam engines and finally by an electrochemist toiling in the laboratory. It was first elucidated and stated by Dr. Julius Robert Mayer (11/25/1814) [5,6]. During his teen age youth, as he grew up by a river in Germany, and tried repeatedly to use an Archimedean screw to pump water back up to the village homes. But, there was not enough energy for that.

In fact, as every experimenter before or since looking for ‘excess energy’ has found (except with CF/LANR), one cannot even recover the energy that is put in: there is no ‘free energy’. This failure of repeated effort would come back later to make Dr. Mayer “discover” the First Law of Thermodynamics. Later, Mayer trained as a physician, at the Eberhard-Karls University graduating in May 1832. But Mayer and his friends (un)fortunately took a “wrong” political side in Europe in 1837 and exposed it openly by wearing forbidden colors (“couleurs”). He was arrested, found guilty, incarcerated, and Mayer was banished for one year. During this time, he voyaged to the Dutch East Indies where he practiced surgery/medicine aboard a Dutch ship. At the time, blood-letting was the state-of-the-art for many medical problems, and something caught Dr. Mayer’s eyes. What he saw in the venous blood was very different in Jakarta compared to the color of the venous blood which he had seen in Paris. The color of his patients’ venous blood was always darker in Europe than Jakarta. He reasoned that this was because less energy was exerted, and, therefore, less oxygen was extracted from the venous blood [5]. Therefore, there is less of an expected color change. This can be seen in Figure 4 where hemoglobin (encased in a polymer by the author) changes color as oxygen is removed; changing from orange-red to purple red [7,8]. Mayer therefore concluded that Europeans used more energy, extracting more oxygen. This energy control and conservation impregnated his thinking as had his failures with the Archimedes screw.

Soon thereafter, Julius Robert Mayer examined both energy and plants more closely. He noted that biological photosynthesis and oxidation as the primary sources of energy for living systems involved the plants converting light energy into chemical energy and work. He articulated the law of the conservation of energy, the First Law of Thermodynamics. In 1841, he wrote “On the Quantitative and Qualitative Determination of Forces” [9] and stated that “energy can be neither created nor destroyed”. One of his first reviewer/referees, Tübingen physics professor Johann Gottlieb Nörreberg rejected Mayer’s hypothesis and noted that if Mayer was right then kinetic energy, such as by vibration, would heat water. Mayer did that experiment, and showed by public demonstration these were connected. This paper was published in May 1842 in *Annalen der Chemie und Pharmacie* which have the value of the equivalent of heat very close to what is measured today [9]. Mayer was spot on. He then derived the relation between the specific heat at



Figure 1. A Classic Philosopher, a Physician, an Engineer, and an Electrochemist Deconvolved the “Laws” of Thermodynamics - (from left and clockwise): Aristotle, Dr. Julius Robert Mayer; Engineer Nicolas Léonard Sadi Carnot; Prof. Walther Nernst.

constant pressure and the specific heat at constant volume for an ideal gas. The relation is:

$$C_{P,m} - C_{V,m} = R \quad (1)$$

where $C_{P,m}$ is the specific heat at constant pressure, $C_{V,m}$ is the specific heat at constant volume and R is the gas constant [10]. This important relation was needed to derive accurately the First Law. However, in response for his clear understanding and explanation of physics (while being a Doctor of Medicine, presumably), Mayer was viciously attacked by many including James Joule and Hermann Helmholtz.

This was shortly followed by attempted plagiarism of his idea by Joule, and finally acceptance of his idea by everyone [11]. Energy was conserved, and Mayer nailed its revelation and its understanding.

Standard Hemoglobin Optical Signatures - These are the colors, and the locations of the optical peaks of hemoglobin, and the optical signatures clearly showing the color change from increasing removal of ambient oxygen [7]. Shown are the optical signatures of d6electronic deoxy-hemoglobin (#1, pH 7.2), d6-oxyhemoglobin (#2, pH 7.2), and d5methemoglobin. Chemical reduction was achieved, and assayed by, sodium dithionite.

3.2 Definition of, and Origin of, the Concept of Energy

Now we must focus on an important, often ignored, matter. Exactly what is this thing called “energy”, that is conserved. The origin, mathematically, of energy conservation is the homogeneity of time which requires that the Lagrangian in a closed system must not depend upon time. Therefore, when the time derivative is taken, with manipulation, a term -defined as the energy - remains a constant [12].

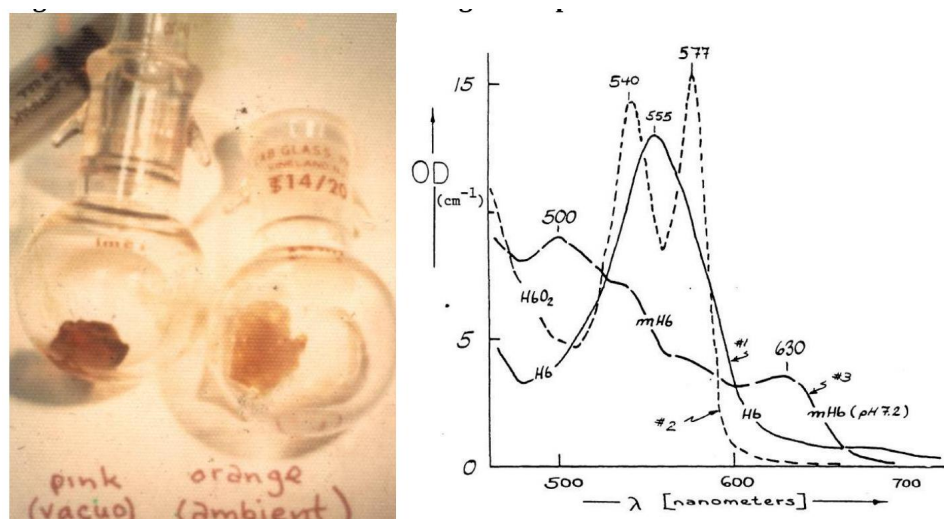


Figure 2. Colors of the Human Hemoglobin Species [after Swartz [ref. 7]]

Table 1. Colors of Hemoglobin (these are dependent on the oxygenation)

Species	Macroscopic color	Peak	Absorptions	[7,8]
deoxyhemoglobin	purple-red	429	555	650 nm
oxyhemoglobin	red-orange	413	540	577
carbonmonoxyhemoglobin	bright red	418	538	570
sulfhemoglobin	green	540	620	
methemoglobin -acid pH	brown	404	500	615
methemoglobin -neutral pH	brown	404	500	630
methemoglobin -alkaline pH	orange-brown	440	540	576 632
cyanmethemoglobin	yellow	418	541	

The relevant equations are thus, where E is the energy:

$$\frac{d}{dt} \left(\sum_i \dot{q}_i \frac{\partial L}{\partial \dot{q}_i} - L \right) = 0. \quad (2)$$

$$E \equiv \sum_i \dot{q}_i \frac{\partial L}{\partial \dot{q}_i} - L \quad (3)$$

In summary, what is taught today in elementary physics courses is conservation of energy -claimed by the First Law of Thermodynamics- and that means that energy can neither be created nor destroyed in a completely isolated system – but can only be changed to other forms. Therefore, as a corollary, the important notion of “energy balance” is also claimed by the First Law of Thermodynamics.

As Mayer noted, this relationship equalizes quantities, and their changes, in mechanical kinetic and potential energy systems, and chemical potential systems, and also their relationship to work. The First Law of Thermodynamics specifically states that the change in internal *energy* of a system is equal to the difference between the heat added to the system, the heat flow out through any barriers, and the work done by the system [1]. Some systems also have different

ways to do work including a mechanical spring, a pulley to raise a weight, or an electric motor. And the work may also include chemical reactions, loading palladium, magnetic strains in a material, and changes in surface energy. Thus, a more general form of energy balance includes the effects of heat transfer and internal energy changes. Therefore the relationship to CF also includes that we as scientists must actually use an even more general form which includes other forms of energy including electrostatic, magnetic, strain, and surface energy [13].

3.3 Classical Thermodynamic Equilibrium Parameters

Classically, thermodynamics is built upon knowledge of the equilibrium parameters involving temperature (T), pressure (P), volume (V), internal energy of the system (U), entropy (S), heat (Q) and work (W). They are related in several ways, and some combinations are important [1]. Most are known to all who studied physics. However, few actually are ever used for calculations, such as in calorimetry, electrochemistry, and electrical engineering. The Internal energy (U) is the kinetic energy of all of the molecules and electromagnetic energy in a system. Q is some of the internal energy which is involved in thermal energy transfer (heat).

The Enthalpy (H) is

$$H = U + P * V \quad (4)$$

The Gibbs Free Energy (G) is

$$G = H - TS \quad (5)$$

The Helmholtz Free Energy is

$$A = U - TS \quad (6)$$

which has “A” which is the work function (Arbeit means work in German).

Today, there are also non-Classical energy parameters. And one of the most important of these in LANR material science is the critical impact of phonons [4]. Some critics incorrectly purport without evidence that quasiparticles and coherent and collective excitations are not real. However, they are quite real and they actually produce many new properties of matter which are quite measurable, such as specific heat, as but one example. The heat capacity of a solid crystal has contributions to energy storage from the phonons, and the excitons, and the plasmons, proving they are quite real, and not imaginary. Furthermore, the phonons are associated with both the metallic lattice, PdD_x, and the aqueous hydrogen lattice, D₂O.

3.4 Energy Transport in Free Space, Vacuum, and Components

Energy can enter a system as work, as heat, and as electromagnetic radiation. The latter is described by the Poynting Vector [15,16,17]. Here, for simplicity and to first order, just the electrostatic contribution is considered. When electrically driving, either the CF/LANR component or system, and/or the ohmic control, both respond with an electrical current across them. As a result, when an electric current passes through an ohmic control (linear time-invariant heater) there is work being done.

With components, assume that the electrical current is constant, and that the component is homogeneous and isotropic so that Ohm’s law is present. Therefore, the electrical current depends upon the electrical conductivity and the applied electric field intensity.

$$J = \sigma E \quad (7)$$

The electrical current being constant means that the electric field intensity is constant, to the degree that there is minimal polarization, so that

$$\text{curl } E = 0 \quad (8)$$

It is also assumed that there is no charge buildup so that

$$\text{div } \mathbf{J} = 0. \quad (9)$$

Hence, the E field intensity produces work by the E-field's interaction upon the charges. Therefore, the induced work dissipates power (work over time), and so, according to Joule's Law.

$$\text{Power dissipated } W = \mathbf{J} * \mathbf{E} = \sigma * \mathbf{E}/2 \quad (10)$$

This is added to the Navier-Stokes equations by differential considerations, and this gives a differential amount of power, in the differential volume, predicated on the mass and specific heat capacity.

$$dW = \mathbf{J} * \mathbf{E}dV \quad (11)$$

which in full form must be integrated over the volume, and over time. Many more complications arise from the lattice [18,19] and many are important to successful CF/LANR.

Energy and Power Losses in Hot and Cold Fusion Systems

As initially discussed by Prof. George Miley [20], power loss in fusion systems can involve other losses. The literature cites many components. Power loss from fusion systems (P_{LOSS}) has the usual components of radiation (P_{RAD}), conduction (P_{COND}) and convection (P_{CONV}). The power loss from radiation (P_{RAD}) as usually considered in hot fusion systems to consist of radiation components secondary to Bremsstrahlung (P_{BREM}), cyclotron radiation (P_{CYC}), and optical emissions (P_{OP}). Furthermore, in cold fusion systems, these must be augmented by three additional terms, which represent additional effects of conduction and convection. As George Miley has shown these include blackbody power emission (P_{BB}), heat (enthalpy) conduction (P_{ENTH}), and the power loss which results through the exit gas stream (P_{GAS}).

The heat conduction in hot fusion is usually handled through its implicit incorporation in the energy confinement time. Here, in LANR, it is included explicitly in equation 1 because the excess enthalpy of cold fusion is the major signal of the desired reactions where phonons play a significant role in hybridized lattices and their electronic behavior.

$$P_{LOSS} = P_{RAD} + P_{COND} + P_{CONVECT} = P_{BREM} + P_{CYC} + P_{OP} + P_{BB} + P_{ENTH} + P_{GAS} \quad (12)$$

3.5 Bremsstrahlung in Fusion Systems

Bremsstrahlung [13, 21, 22] is most important to LANR since 1989 especially given the alleged 'graduate student problem' [23]. Bremsstrahlung radiant power from cold fusion differs from hot fusion in being markedly lower in intensity, with an output spectrum in the near infra-red. In hot fusion, significant levels of Bremsstrahlung occur at hot temperatures characteristic of plasmas. Because of the energies involved, the Bremsstrahlung radiation is penetrating and cannot be contained.

This is important because at relativistic energies, the energy loss by Bremsstrahlung may exceed that secondary to all collision interactions with matter surrounding and within the reactor. In hot fusion systems, the energetic ions and electrons of the plasma radiate so much ionizing (x-ray) power by Bremsstrahlung that this radiation leakage challenges reactor planning. To explain this much more clearly, the following goes into this physics in detail.

Bremsstrahlung [Breaking Radiation]

Bremsstrahlung, described by a theoretical energy spectrum and angular distribution [22,23], has an observed power output spectrum as a function of the emitted photon energy. The output spectral curves are continuous, and also

contain characteristic material-specific photon peaks (lines) superimposed. The latter occurs from the displacement of lower-lying electrons in the target and the subsequent refilling of those orbitals.

There are two well-known types of Bremsstrahlung - outer and inner. Outer Bremsstrahlung is the release of ionizing radiant energy from highly energetic moving charged particles upon their deceleration [20,21]. This form of Bremsstrahlung was first observed when it produced secondary x-radiation from fast moving electrons hitting thick metallic targets. Inner Bremsstrahlung occurs in β -decay and results in the emission of photons in energy between zero and the maximum energy available for that transition. Inner Bremsstrahlung, double Bremsstrahlung [26]–[28], polarization Bremsstrahlung, solar Bremsstrahlung [29] and the relativistic Bremsstrahlung associated with hadronic showers including solutions by the Weizsacker-Williams method of virtual quanta will not be discussed in this paper.

Bremsstrahlung Radiation Cross section

The energy in the Bremsstrahlung output spectrum is expressed for incident beam or Gedanken experiments as a cross section of photon emission [13]. This enables the determination of the beam energy loss as a function of distance $[\frac{dE_{rad}}{dx}]$. The radiation cross section of Bremsstrahlung has been considered several ways including classical, semiclassical quantum, and the Bethe-Heitler quantum mechanical Born approximation (done in 1934). Calculations usually begin with the kinetic energy of the moving particle considered, relativistically if necessary [30, 16, 31]. The emission of Bremsstrahlung radiation is most important for low mass (m) particles impinging upon high atomic number materials (Z_M), and therefore for electrons impinging upon palladium ($Z = 46$) or nickel ($Z = 28$).

If N is the number of fixed charges in a unit thickness, the energy loss per unit distance becomes

$$\frac{dE_{rad}}{dx} = N \int \chi(\omega) d\omega \quad (13)$$

Equation 13 is solved by use of conversion to a new variable of integration, $x = \frac{h\omega}{2\pi E}$. The radiative loss per unit distance by Bremsstrahlung is thus

$$\begin{aligned} \frac{dE_{rad}}{dx} &\cong \frac{16}{3} N * \left(\frac{2\pi Z_M^2 e^2}{hc} \right) * \left(\frac{z^4 e^4}{Mc^2} \right) \\ &= [32/3] * N * \pi * [Z_M^2] * [e^6/hc^3] * [z^4/M] \\ &= \frac{32}{3} N \pi Z_M^2 \frac{e^6}{hc^3} \frac{z^4}{M} \end{aligned} \quad (14)$$

Screening Effects for sufficient relativistic energies

Screening effects due to the target atomic electrons have not been considered above, but are typically included through their relationship to the impact parameter [13]. There is a critical energy (E_s) beyond which the impinging relativistic particles are said thereafter to have “complete” screening. The important result from screening considerations, discussed elsewhere, is that for all $E > E_s$, the Bremsstrahlung radiation cross section changes and, thereafter for increasing frequencies, becomes constant. Where does this occur for the materials used in cold fusion? For beam systems where this has been experimentally confirmed, for electrons in aluminum ($Z = 13$) this critical energy, E_s , is about $\sim 42\text{MeV}$, and for lead ($Z = 82$), the relevant relativistic energy E_s is $\sim 23\text{MeV}$. This is characterized by

$$E_s = \left(\frac{192M}{z^{\frac{1}{3}} m} \right) Mc^2 \quad (15)$$

Equation 15 was used to calculate the expected critical energy (E_s) for the hydrided materials associated with cold fusion. For electrons in palladium ($Z = 46$), this calculation is $E_s \sim 28\text{MeV}$. For nickel ($Z = 28$), it $E_s \sim 33\text{MeV}$, and titanium ($Z = 22$), $E_s \sim 35\text{MeV}$. The important relevant conclusion is that the Bremsstrahlung screening effect is unimportant in this analysis of cold fusion systems.

Calculation of λ_{\min}

By inspection, conservation of energy requires that the maximum wavelength of Bremsstrahlung emission be limited to, under non-relativistic conditions, the kinetic energy of the incident particle, and so $\frac{hc}{\lambda_{\min}} \cong \frac{1}{2}Mv^2$. This has great impact upon radiation behavior[13]. The upper limit for photon energy emission occurs at the shortest wavelength [Angstroms] which is inversely dependent upon the voltage (V) used.

$$\lambda_{\min} = \frac{hc}{eV} = \frac{12,396}{V} \quad (16)$$

The Bremsstrahlung of cold fusion differs from hot fusion due to the lower temperature. At cold fusion temperatures, circa 300 K implying equivalent energies of 1/40 electron volt, the maximum energy (minimum wavelength) output of Bremsstrahlung emission is in the near infra-red. Given this result, the most important implication is that cold fusion Bremsstrahlung would have insignificant penetration of the electrode or even aqueous medium. The penetration depth, and its implications, will be calculated after first considering the relative role of Bremsstrahlung radiation to all collision related energy losses.

Final Bremsstrahlung Output Power Calculation

The standard calculation for plasma and hot fusion Bremsstrahlung requires determinations of both ion density and excitation energy [13,32]. The Bremsstrahlung power equation becomes

$$P_{BR} = 5.35 \times 10^{-31} f \sum_j k_j Z_j^2 * (n^2) * T^{e \frac{1}{2}} \quad (17)$$

where $f = \sum_j k_j * Z_j$ the electron temperature is T_e (in keV), and there are n ions/cm³, containing j nuclear species, of charge Z_j and of fraction density (sum = 1) of $k_j * n$. Here, Z is the nuclear charge, n_i and n_e are ion and electron densities (number of particles /cm³) and T is the electron temperature [keV].

Important Metric of Radiant X-ray Power

First, the Bremsstrahlung radiant x-ray power volume is much less at cold fusion (CF) temperatures (~ 300 K) than at thermonuclear temperatures. However, the determination as to whether Bremsstrahlung is important for CF (as it is for thermonuclear fusion) also depends upon the ratio of Bremsstrahlung power to fusion power. In kinetic beam experiments as discussed above, it is also important to consider the radiant x-ray power in comparison to input electrical beam power. In the sense that cold fusion experiments also have central electrical input power distributions as the etiology of the fusion mechanism, this factor was also examined for the case of cold fusion.

$$\eta = \frac{x\text{-ray power}}{\text{beam power}} = 0.0007 * Z * V \quad (18)$$

The ratio of x-ray power to beam power falls from 0.05–0.28 (hot fusion, characterized by aluminum and lead targets, Table 1) to $1.4 - 8.1 \times 10^{-10}$ for cold fusion [palladium $Z = 42$, and water (average $Z = 8$)]. This marked decrease in the exit of ionizing Bremsstrahlung radiation is directly reflected in the irradiation dose delivered. This

can be calculated [13] from the x-ray beam dose equation [32], here modified as the x-ray dose in Grays (at 1 meter) delivered per coulomb of electrical input.

$$D/Q = 1.50 * V_{\max}^{2.8} Z^{1/2} \text{ [Grays/Coulomb]} \quad (19)$$

V_{\max} here is dominated by $k_B T$ because the applied electrical field intensity, assuming homogeneous distribution over the system is insignificant by comparison. This most important result from equations 18 and 19 is the correct calculation that the derived value of the Bremsstrahlung delivered dose at a distance of 1 meter is some 11 to 18 orders of magnitude less than that expected for conventional fusion systems.

Most importantly, the irradiation dose (Grays) per coulomb at 1 meter drops from 3.1×10^{19} Grays (hot fusion) to $1.4\text{-}3.3 \times 10^{-4}$ Grays for cold fusion [13].

[embolden for emphasis below it.]

This result is consistent with experimental findings over more than three decades. Again there is no reason for the experimenters in cold fusion laboratories to have easily seen any ionizing radiation because, like neutrons, there are theoretical reasons for x-radiation to be absent. Some recent experiments are consistent with cold fusion (using the codepositional method) producing very low levels of ionizing energy release in the range of ~ 6 to 30 keV [33,35]; and for emissions from NANOR-type components [34,36].

3.5.2 Implication of Shift to Nonionizing IR Output

We have closely examined the impact of the fact that Bremsstrahlung radiant power exists, in cold fusion systems, in the near-infrared [13]. The shift of the cold fusion Bremsstrahlung output power spectrum to non-penetrating radiant energies has great implications. The first implication of the maximum energy with cold fusion is the increase in the role of self-attenuation. As an example of how significant this effect might be, consider that small amount of even low-Z filtration produces the well-known effects of beam hardening widely used by radiologists for a century. For example, when 65 keV electrons are bombarded into tungsten targets, the filtering of 1 mm aluminum alone cause all radiation below about 10 keV to drop to virtually zero.

The second implication is effective containment of the radiant Bremsstrahlung power, and its overlap with thermal and phonon processes[13]. With cold fusion, could the impact of this present serious and interesting physics because of the extremely limited skin depth? It must be true that the final boundary condition will be the StefanBoltzmann distribution of blackbody radiation characterizing the system.

However, in this case, there is the additional, albeit small, localized input from the cold fusion Bremsstrahlung radiation which may act to supplement the local phonon field.

IMPACT OF SKIN DEPTH

The loss of potential fusion energy through Bremsstrahlung radiation is very low for cold fusion systems because the radiation is in the near infrared and, therefore, is trapped by the skin depth effect to remain vicinal to the reactions[13]. The infrared radiation is essentially locked into the materials, as opposed to the penetrating, uncontained, ionizing radiation of hot fusion. The energy transfer in cold fusion through Bremsstrahlung is limited by the skin depth which is relatively small. The skin depth is defined, in continuum terms, where σ is the conductivity, and μ the permeability, by

$$\delta_{\text{skindepth}} = \frac{2}{\sqrt{\omega * \mu * \sigma}} \quad (20)$$

For palladium (9.25×10^6 mhos/meter), at 1 Megahertz this is 0.066 mm, but in the infrared [$10^{13} - 6 \times 10^{14}$ Hz], the skin depth ranges from 2.7 to 20.9 nanometers. This must be compared to the hot fusion Bremsstrahlung which is very penetrating with tenth value thicknesses of lead ranging from 0.2 to 65 millimeters.

The result of equation 20 is that because of the skin depth, the energy of the Bremsstrahlung radiation is trapped inside the metal, possibly in thermodynamic equilibrium, and can only exit by blackbody radiation, exit gas stream (or possibly monatomic gases, or ions, through catastrophic desorption) or further phonon conduction.

Possible Secondary Effects

Most importantly, the lock-in effect means that there may be additional post-fusion contributions to the optical and acoustic phonons. These lattice vibrations have coupling in the infrared, which itself is linked with molecular vibrations. Given the lattice, additional phonons would thereafter develop. To the degree that these phonons are needed to continue further CF reactions, the cold fusion Bremsstrahlung might accelerate the desired reactions.

3.5.3 Summary Analysis of Bremsstrahlung

It is important to summarize these very important results.

We have examined the role of Bremsstrahlung in cold fusion systems [13]. The results show why those figurative cold fusion graduate students never died, unlike hot fusion or plasma systems. The reason the graduate students, and CF/LANR researchers were saved. The reason why is that we calculate that there is a VERY marked shift in Bremsstrahlung power density compared to beam power, from 0.05-0.28 (hot fusion) to $1.4 - 8.1 \times 10^{-10}$ for cold fusion [palladium $Z = 42$, and water (average $Z = 8$)].

As a result, the delivered x-ray beam dose (at 1 meter) decreases by 11 to 18 orders of magnitude as the irradiation dose (Grays) per coulomb drops from 3.1×10^{19} Grays (hot fusion) to $1.4-3.3 \times 10^{-4}$ Grays for cold fusion.

Attention is directed to the fact that these calculations, based upon temperature, are consistent with the relative absence of apparent ionizing emissions from cold fusion systems except for a few reports looking in the ~ 6 to 20 keV region.

Most importantly, the Bremsstrahlung radiant power from cold fusion differs from hot fusion in that - because of the markedly lower temperature - most of the Bremsstrahlung radiant power in cold fusion systems is in the near-infrared region.

This occurs because the energy transfer in cold fusion systems via Bremsstrahlung radiation is limited by the skin depth which for palladium (9.25×10^6 mhos/meter), in the near infrared [$10^{13} - 6 \times 10^{14}$ Hz] ranges from 2.7 to 20.9 nanometers. This is important because the lock-in of cold fusion Bremsstrahlung has important secondary effects upon the rates of the desired fusion reactions. One very important implication for CF/LANR is that the effective containment of the radiant Bremsstrahlung power, and its overlap with thermal and phonon processes [37-39].

3.6.1 Application of First Law: Energy Conservation in Calorimetry

Now we come to the role of energy conservation in calorimetry. Until the development of LANR detection systems like coherent antiStokes CMORE spectroscopy [37-3] and Deuterium-line RF emissions [40-42], CF/LANR investigators have had to rely solely upon calorimetry (and occasional mass spectroscopy when very lucky to look for de novo ^4He). Calorimetry will remain the mainstay for a long while.

In calorimetry, there are several important types [43-50]. When pressure remains constant, it is an isobaric process. When temperature remains constant, it is an isothermal process. When there is no exchange of heat between the gas and the environment, it is an adiabatic process. More commonly in this field, there is a constant volume while the pressure is free to change. This is an isovolumetric or isochoric process.

An isoperibolic system is a system in which the controlling external temperature is kept constant.

Calorimetry by Conservation of Energy and Mass

For analysis, for each type we must consider the specific heat of water, and use NavierStokes analysis to examine the flow of matter and energy [50]. Another advantage of using this method is that it is valid always. By contrast, the Nernst equation is not even valid unless there is equilibrium which is why the very successful quasi-1-dimensional model of loading was developed [14].

3.6.2 Derivation of Navier-Stokes Equation

The Navier-Stokes equation is derived from $F = ma$, which is conservation of momentum and from the equations for conservation of mass and energy. Conservation of mass requires the continuity equation [50].

- Conservation of momentum

$$m\vec{a} = \sum \vec{F}$$

mass
acceleration
Sum of all forces acting on fluid

(21)

- Conservation of mass (continuity equation)

$$\nabla \cdot \vec{v} = 0$$
(22)

- Conservation of Energy

$$\rho c \frac{\partial T}{\partial t} = k \nabla^2 T + \dot{q}$$

Rate of change of local heat energy stored
heat conducted out
heat generated

(23)

Navier Stokes equation

$$\rho \left[\frac{\partial \vec{V}}{\partial t} + (\vec{V} \cdot \nabla) \vec{V} \right] = \rho \frac{D\vec{V}}{Dt} = -\nabla p + \rho \vec{g} + \mu \nabla^2 \vec{V}$$

Convective derivative
Convective derivative
Pressure
Gravity
Diffusion

(24)

The increment in internal energy (enthalpy) per unit mass is $c_v dT$ for an ideal gas where c_v is the specific heat at constant volume. $c_p dT$ is the incremental change in enthalpy per unit mass at constant pressure.

The desired equations add the forces on the right-hand side of Equation 24, here being force(s) which arise from a pressure gradient, from gravity, and diffusion. Finally, because this is a Euler equation (a flow through a volume) rather than a Lagrangian [such as where the ball is thrown, as a $f(x, y, z)$], the convective derivative is needed and used on the left-hand side of Eq. 24 .

3.6.3 Benard Instability, and the Boussinesq Approximation

In some cases of flow calorimetry, the thermal expansion of the involved fluids must next be addressed. The key problem is that water and air and other fluids used in flow calorimetry suffer from thermal expansion. Their density is

a function of temperature. Thus, water when it freezes floats on top, as one example, thereby fortunately saving all of the life below in the pond during the Winter.

For simplicity, the Boussinesq approximation is used, which only considers the thermal expansion in any term of Eq. 4 involving gravity (such as on the right hand side). Solution leads to Benard instability, the Rayleigh Taylor wavelength, and what is universally observed in continuum electromechanics [51]. This equation is generally ignored in simplistic flow calorimetric systems/calculations.

η_B Evaluates Impact of Buoyancy Effect

We derived a non-dimensional number ($= \eta_B$) which can determine if flow calorimetry is defective when it is significantly greater than zero, and can be used to correct the flow calorimetry to the first order [52-56].

η_B is the ratio of heat transported by the buoyant forces to the heat transported by the applied solution convection.

η_B is also derivable from other non-dimensional factors including the Archimedes non-dimensional number (which is the ratio of the buoyant force to the viscous force), and the Rayleigh non-dimensional number (which is the ratio of gravity to thermal conductivity).

3.6.4 First Order Correction for Buoyancy Factor

To zeroth order one can write using the specific heat capacity, the temperature differential, and the rate of mass transfer caused by both the expected convection and the buoyancy movement secondary to the temperature inhomogeneity [56].

$$P_{\text{observed}} = P_{\text{out}} + P_{\text{error}} = C_p * \Delta T * V_{\text{total}} \cong C_p * \Delta T * (V_{\text{convection}} + V_{\text{buoyancy}}) \quad (25)$$

The chain rule in calculus and consideration of coolant redistribution reveal the higher order terms from the impact of the buoyant flow.

$$\frac{\delta P_{\text{error}}}{\delta \eta_B} = (C_p * \Delta T * V_{\text{convection}}) + \left(C_p * V_{\text{convection}} * \eta_B * \frac{\delta \Delta T}{\delta \eta_B} \right) \quad (26)$$

The term containing $\frac{\delta \Delta T}{\delta \eta_B}$ depends upon many factors including the total tank volume just outside the reactor (or thermal control) and the actual input temperature boundary condition. However, that term appears to be higher order, and so the linear correction to the observed power becomes

$$P_{\text{corrected}} = P_{\text{observed}} - (C_p * \Delta T * V_{\text{convection}} * \eta_B) \quad (27)$$

An improved estimate of the purported gain (or over-unity gain) then becomes, corrected to first order [56],

$$P_{\text{corrected}} = P_{\text{observed}} * (1 - \eta_B) \quad (28)$$

This important result means that the semiquantitative corrected Incremental Power Gain of these experiments is equal to the indicated Incremental Power Gain times $(1 - \eta_B)$.

3.7 Limitation of the First Law

That said, there are limitations of First Law. They are VERY important for cold fusion by any name (CF/LANR/LENR). First, the First law cannot even indicate if a reaction(s) is spontaneous, or its rate, or the direction of heat or deuteron flow, nor will it provide information about final temperatures or concentrations or distributions, or information on the entropy. Electrical engineering of applied fields and Navier-Stokes models with convective derivatives are far more useful.

Second, in addition, the first law of thermodynamics cannot determine or distinguish which direction heat flows between a cold object and a hot object. Yet we observe the heat flows in one direction only - heat only flows from a hot body to a cold body.

4.1 Second Law of Thermodynamics - Entropy Always Increases

The Second Law of Thermodynamics declares that entropy will always increase, which for most things of large number is quite reasonable [1]. Entropy is a thermodynamic parameter, symbol S , describing disorder in a system or in a material. Entropy is disorder but it heralds more. The availability and accessibility of energy depends on entropy. It is more difficult to access energy as the entropy increases. The origin, limitations, and other issues of the Second Law are described in detail below.

The change in entropy during a thermodynamic process is defined as:

$$\Delta S = \int dQ/T \quad (29)$$

Thus, going back to electrical heating, the total entropy increase is defined as

$$dS/dt = \int (J^*E)/T dV \quad (30)$$

4.2 Origin of the Second Law of Thermodynamics

The Second Law of Thermodynamics was derived by the French physicist Nicolas Léonard Sadi Carnot in 1824 [57]. He was a French engineer trained at the École Polytechnique in Paris by Joseph Louis Gay-Lussac, and André-Marie Ampère. His classmates were Claude-Louis Navier and Gaspard-Gustave Coriolis, and with them Carnot studied steam engines. Carnot died of cholera at 36, and his writings were buried alongside him.

In those days, heat was viewed as an invisible flowing liquid. In 1824, Carnot published *Reflections on the Motive Power of Fire* [58, 59] postulating the Carnot cycle and first discussed the idea of “reversibility” where work would give a temperature rise. Carnot’s work showed there are losses in work, from entropy, and only its absence yielded the upper limit of efficiency of converting heat to work [60–63]. He demonstrated that the maximum thermal efficiency of a heat engine occurred when all the heat supplied was at a constant temperature (T_1), and when all the work was conducted at a constant temperature (T_2). The maximum thermal efficiency was related to both and is

$$\eta_{\max} = 1 - ((T_1) * (T_2)) \quad (31)$$

This is an alternate equation from the second law of thermodynamics. The equation was very useful since the efficiency of steam engines was 3%.

4.3 Limitation of the Second Law

The Second Law of Thermodynamics is not a “Law” as much as it is a statement of probability. The Second Law of Thermodynamics purports that the state of entropy of an isolated system will increase over time, but there are many limits to it. Two examples are shown below.

First, entropy involves large numbers of particles/systems, so this cannot refer to Lagrangian single particle. Cohorts must be used, resulting in probabilities. Thus, sometime small numbers of particles can break the Second Law, but large numbers make breaking the Second “law” extremely unlikely.

Second, another weakness of the “law”, is that the Second Law states that the time rate of change of the entropy can never be negative over the Universe, but locally, over a small volume, biology, and artificial intelligence and advanced materials demonstrate that THAT “law” may not be always true.

4.5 Entropy in Language [Including Discussions of CMNS]

Entropy from the Second Law is relevant to CF/LANR even when we and our colleagues speak about it. This is why: Entropy is the metric used to measure uncertainty in both physics and in languages (“communication”). In the latter, entropy refers to the amount of randomness of speech or text, and failure to communicate.

To understand this quantitatively, consider that the goal of any language is to transmit information. The amount of information in a message is denoted by the “entropy”, as proposed by Claude Shannon [64,65]:

“The entropy is a statistical parameter which measures, in a certain sense, how much information is produced on the average for each letter of a text in the language.”

[“Prediction and Entropy of Printed English”].

Shannon’s entropy is a measure of uncertainty. The higher the entropy, the more frequent are communication errors. This is how it is related to speech and text. Language performance is measured by perplexity, cross entropy, and bits-per-character (BPC), and accuracy. Perplexity reflects the uncertainty. Perplexity as metric shows if a probability distribution or probability model actually will predict an accurate result. The actual crossentropy is greater than the calculated entropy because it involves an additional loss from coding and/or recognition for logistic regressions and artificial neural networks.

Bits-per-character and bits-per-word are the metrics used which enable determination of Shannon’s definition of entropy. Entropy is also directly proportional, to first order, to the maximum attainable data speed transmission rate [in bps (bits per second)]. Entropy is also the average number of binary digits required per letter of the original language to translate each letter in a most efficient way.

“If the language is translated into binary digits (0 or 1) in the most efficient way, the entropy is the average number of binary digits required per letter of the original language.”

[“Prediction and Entropy of Printed English”].

The entropy of a language is an estimation of the probabilistic information content of each letter in that language and so is also a measure of its predictability and redundancy. Entropy of a language thus becomes a statistical parameter which measures, in a certain sense, how much information is produced on the average for each letter of a text in a language. In language, some words always are linked with others, and this effects the entropy. This additional relationship/linkage is important because the probability is linked to the preceding word/symbol.

5.1 The Third Law of Thermodynamics

The Third Law of Thermodynamics was formulated by the German chemist Walther Nernst in 1906 [66-69]. The Third Law of Thermodynamics purports that the entropy of a system approaches a constant value as the temperature approaches absolute zero, and that value for all perfectly crystalline solids is zero at the absolute zero temperature [“perfect order in a crystalline solid”].

Many problems in electrochemistry and CF/LANR in particular have arisen from the Nernst equation. These have been discussed by Herbert Uhlig [70], and there are major differences with other electrochemists who relied only on the Nernst equations [70,71]. The issues are beyond this paper and have been covered elsewhere [14]. The most important point is that these things are known and the Nernst equation is only relevant at equilibrium whereas active CF/LANR systems and components are definitely not at equilibrium [14].

5.2 Limitation of the Third Law

There are limitations of Third Law of Thermodynamics. They may be important for cold fusion. Several things do not fit this including glassy solids, mixtures of isotopes of a single element, and some simple molecules including CO, N₂O, NO, H₂O, and probably heavy water. Each has an entropy greater than zero at absolute zero. This will be shown by way of water, and heavy water. Water is described here because of its entropy, and how it demonstrates that the Third “Law” fails. First, a thermodynamic review of water, and its lattices [72,73].

5.2 Water - Critical to LANR and many Calorimeters

Water has a great heat capacity with a negligible increase in temperature [72]. It is the deuterogen bonds, and the diversity of structures available to water, which accounts for this important phenomenon [72-78]. High boiling point is another corollary. The origin of the heat capacity is the entropy discussed below.

There are Two Lattices in Water and Ice

Water has a three dimensional stereoconstellation, and surprisingly it has both order (the oxygen atoms) and disorder (the protons or deuterons) [73]. Water’s atoms of oxygen and hydrogen (or deuterons) are arranged in structures with definite physical rules and it is best understood as a complicated three-dimensional structure comprised of two lattices. The lattice of the protons and/or deuterons is located within a second lattice (the oxygen atoms). The most important point is that there are two lattices and that the proton lattice is often totally ignored. Much has been learned by studying the protons, their electric dipole moments, and their entropy, which results from their distribution and decoration upon the organized oxygen lattice [73].

The fact that water has a second proton lattice within it means that water has not only singular properties, but has an incredible impact upon both the properties of materials dissolved within it (including clathrates, hydrates, biological systems, etc.) and the operation of systems using it. Additional complexities occur because the hydrogen in water could be the rarer heavy hydrogen, deuterium, which is the desired fuel in CF/LANR and is used at 99 to 99.95% purity levels in the best CF/LANR systems.

Hydrogen/Deuteron Bond

The immersion of a hydrogen, actually the proton, into an electronic cloud of a neighboring water molecule begins the process toward understanding water/ ice structure. The H -bond process consists of that immersion of one proton into the electronic cloud of a neighboring oxygen acceptor. A wide range of angles are possible for the lone electron-pair acceptor. The coulombic neutralization yields an energy decrease in the order of 4.5kcal/mole ($k_B T = 0.6\text{kcal/mole}$). What occurs when the hydrogen bond is formed is that a thermally-stable structure results and an electric dipole moment is formed [72-76]. The bridge dipole is a simplification, because it is actually a superposition of individual dipole moments. Each bridge consists of two dipoles. The vector sum can be associated with each bridge.

The deuteron bond, similar to the “hydrogen bonds” of light water, decisively controls this materials aggregation properties. This occurs because of the ratio of the energy involved in a deuterogen bond (~ 4.5 kilocalories per mole) versus the lesser, albeit omnipresent, thermal energy [$k_B T$] which is only 0.6 kilocalories per mole. The result is that thermal energy [$k_B T$] is insufficient to disrupt more than a statistically few deuterogen bonds at any given time [73].

5.3 Deuteron/Proton Disorder in the Condensed Phase

The oxygen lattice is strictly ordered, but it is important to know that the proton sublattice is disordered. The proton disorder of water’s hydrogen sublattice leads to the unusual electric conduction and polarization properties of water.

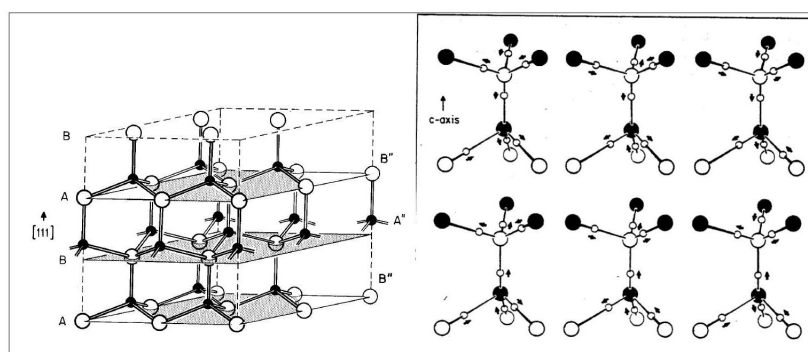


Figure 3. (left) Ordinary ice (Ice 1h) lattice showing the oxygen nuclei in hexagonal arrangement. The Wurtzite-type structure of Ice 1 h showing the lattice which creates an open optical (c-axis) axis, viewed best using crossed polarizers, consisting of tetrahedral H₂O molecules held in a proton-disorder stereoconstellation [72–78]. Contained within the ordered oxygen tetrahedral lattice is the disordered proton sublattice. The disordered results from the fact that every oxygen bridge has two (2) nearly equivalent proton positions. (right) Possible arrangements of protons in water. Shown are the six possible arrangements of protons in a Wurtzite-like (eclipsed) Ice 1h structure composed of eight water molecules.

Most importantly, the proton disorder creates the large dielectric constant of water that enables water to dissolve so many materials. Furthermore, the proton disorder of water/ice contributes to the great heat capacity of water {the ability to absorb heat with a negligible increase in temperature}.

Figure 3 shows 6 possible configurations which can exist for two oxygen nuclei. Because these are indistinguishable, there are only 3 such configurations [72,73-75]. Furthermore because each layer eliminates randomness from the next layer there are $3/2 = 1.5$ arrangements. The calculated entropy, therefore is

$$S = k_B * \ln (\text{Number of states}) \quad (32)$$

Examining the form of ice, thus the entropy S is:

$$S = R * \ln(1.5) = .81$$

Note that this calculated value is indeed very close to the measured value of .82 calories/gram-mole.

This entropy for water-ice, calculated here to high accuracy, does not follow the Third “Law” at absolute zero temperature, but lessons remain none-the-less.

6. Conclusion

Thermodynamics is our best, constantly developing, engineering method to study the inter-relationships and multiple (re)-conversions between heat and several types of energy; both in the world around us, and in the local version within our CF/LANR experiments. Thermodynamics is fundamental, but as shown here, it must be tempered and considered alongside both actual engineering and material science realities. Together, their science is the proven way to excellently understand it better toward our goal(s) of achieving better working, more reproducible cold fusion (LANR) systems with higher incremental power gain and power density.

In lattice assisted nuclear reactions (LANR) systems, thermodynamics controls electrodes, explains diagnostics, and limits emissions. Although thermodynamics has several problems, as all limited first-order guess-work analyses do, they are now very well defined, and therefore, discussing its scope, its origins, and its many roles in our measurements will continue to improve the development and engineering of CF/LANR systems.

Acknowledgments

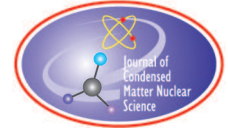
The author gratefully acknowledges, and thanks, for their helpful comments, editorial assistance, ideas, suggestions, and much long term support for this effort: Gayle Verner, Jean-Paul Biberian, and his reviewers, Alex Frank, Joshua Gyllinsky, Susan Woods, Thomas Farina, Michael Staker, John Wallace, Andrew Meulenberg, Brian Josephson, Isidor Straus, Peter Hagelstein, Dennis Cravens, Dennis Letts, Frank Gordon, Pamela Mosier-Boss, Lawrence Forsley, Brian Ahern, Jeff Driscoll, Raymond Kurweil, Aaron Kleiner, Christy Frazier, Win Cuthbert. This effort was supported by JET Energy Inc. NANOR[®] and PHUSOR[®] are registered trademarks. The technology described here is protected by patents pending.

References

- [1] Frederick Reif, *Fundamentals of Statistical and Thermal Physics*, ISBN-10: 9781577666127, Waveland Pr Inc; (2008)
- [2] Richard P. Feynman, Robert B. Leighton, Matthew Sands, *The Feynman Lectures on Physics, Vol. I: Mainly Mechanics, Radiation, and Heat*; ISBN-10: 8131792110 (2011)
- [3] Prigogine, Ilya, *Introduction to Thermodynamics of Irreversible Processes*, New York: Interscience Publishers (John Wiley & Sons), 1968; https://isidore.co/calibre#panel=book_details&book_id=4305
- [4] Swartz, M. R, *Quasiparticles, Collective Excitations and Higher-Order Collective Quasi-Excitations in Lattice Assisted Nuclear Reactions*, *J. Condensed Matter Nucl. Sci. with Excess Heat Mode*, *J. Condensed Matter Nucl. Sci.* 24, 130-145 (2017)
- [5] Julius von Mayer: https://en.wikipedia.org/wiki/Julius_von_Mayer
- [6] Michael Fowler, Robert Mayer and the Color of Blood, <https://galileo.phys.virginia.edu/classes/152.mf1i.spring02/MayerJoule.htm>
- [7] Swartz M.R., “Charge Transfer to Methemoglobin and Oxygen using Methylene Blue, Light and Electricity”, ScD Thesis, Dept. of Electrical Engineering, MIT, Cambridge, MA, (1984).
- [8] van Assendelft, O. W. “Spectrophotometry of the Hemoglobin Derivatives”, Royal Vangoricum Ltd., Netherlands (1970).
- [9] J. R. von Mayer, *Annalen der Chemie und Pharmacie* 43, 233 (1842); Mayer, J. R. (1842). “Bemerkungen Äijber die KrÄd’fte der unbelebten Natur”. *Annalen der Chemie und Pharmacie*. 42 (2): 233-240. doi:10.1002/jlac. 18420420212. hdl:2027/umn.319510020751527; Mayer, J R (1862). “Remarks on the Forces of Inorganic Nature”. *Philosophical Magazine*. 4. 24 (162): 371-377. doi:10.1080/14786446208643372.
- [10] Lehninger, A. “Biochemistry”, Worth Inc. New York (1975)
- [11] Esther Inglis-Arkell, *Why Julius Robert von Mayer was one of the unluckiest men in science*, 2013; <https://gizmodo.com/why-julius-robert-von-mayer-was-one-of-the-unluckiest-m-5985512>
- [12] L.D. Landau & E.M. Lifshitz *Mechanics (Volume 1 of A Course of Theoretical Physics)* Pergamon Press 1969; https://archive.org/details/Mechanics_541
- [13] Swartz, M, G. Verner, “Bremsstrahlung in Hot and Cold Fusion”, *J. New Energy*, 3, 4, 90-101 (1999)
- [14] Swartz, M, “Quasi-One-Dimensional Model of Electrochemical Loading of Isotopic Fuel into a Metal”, *Fusion Technology*, 22, 2, 296-300 (1992)
- [15] Von Hippel, A. Ed., “Dielectric Materials and Applications”, MIT Press, Cambridge (1954).
- [16] Adler, R.B., L. J. Chu, R.M. Fano, “Electromagnetic Energy Transmission and Radiation”, Wiley & Sons, Inc., NY (1966)
- [17] Melcher, J. R., “Continuum Electromechanics”, MIT Press, Cambridge, (1981).
- [18] Kittel, C., *Introduction to Solid State Physics*, 8th Edition, ISBN:978-0-471-4152688th Edition (2004)
- [19] Ashcroft, Neil W., N. David Mermin, *Solid State Physics*, ISBN-13: 978-0030839931, Publisher Brooks Cole (1976)
- [20] Miley, G.H., “Fusion Energy Conversion”, American Nuclear Society (1976)
- [21] Kaplan, Irving, “Nuclear Physics”, Addison-Wesley Publishing, Reading MA (1962); Johns, H.E., Cunningham, “The Physics of Radiology”, Charles C. Thomas Publisher, Springfield, 1953.
- [22] Friedlander, M. W., “Cosmic Rays”, University Press, Cambridge MA (1989)
- [23] Mallove, E. J. (1999). *Fire from Ice: Searching for the Truth Behind the Cold Fusion Furor*, Infinite Energy Press, United States of America, ISBN 1-892925-02-8; Eugene F. Mallove (1991), *Fire from Ice: Searching for the Truth Behind the Cold Fusion Furor*, Wiley Science Editions (illustrated ed.), John Wiley & Sons, ISBN 978-0-471-53139-5

- [24] L.I. Schiff, Phys. Rev. 83.2, 252 (1951)
- [25] J. L. Matthews and R. O. Owens, N.I.M. 157-168 (1973)
- [26] C. Quarles, J. Liu “Review of Two-photon Bremsstrahlung in Electron-atom Collisions,” Nucl. Inst. Meth. Phys. Res. B, 79, 142 (1993).
- [27] C. Quarles, J. Liu, “The yield for two-photon emission from radiation of thick targets by a Cd109-Cd113m radioactive source”, Nucl. Inst.Meth. Phys. Res. A., 337, 127 (1993).
- [28] C. A. Quarles, D. Kahler and J. Liu, “Double Bremsstrahlung”, Phys. Rev. Letters, 68, 1690 (1992).
- [29] Friedlander, M. W., “Cosmic Rays”, University Press, Cambridge MA (1989)
- [30] Heitler, W., “The Quantum Theory of Radiation”, Oxford Clarendon Press (1954)
- [31] Jackson, J.D., “Classical Electrodynamics”, Wiley & Sons, Inc., NY (1962)
- [32] Huba, J.D., NRL Plasma Formulary, Office Naval Research (1994)
- [33] S.Szpak, P. Mosier-Boss, R. Boss, J. Smith, “On the behavior of the Pd/D system: Evidence for Tritium Production”, Fusion Technology (1998)
- [34] Swartz M. R., Incremental High Energy Emission from a ZrO₂ – PdD Nanostructured Quantum Electronic Component CF/LANR, J. Condensed Matter Nucl. Sci. 15, 92 (2015);
- [35] Swartz, M.R., “Survey of the Observed Excess Energy and Emissions In Lattice Assisted Nuclear Reactions”, Journal of Scientific Exploration, 23, 4, (2009) 419-436.
- [36] Swartz M.R., Verner, G., et al., Imaging of an Active NANOR^Å-type LANR Component using CR-39, J. Condensed Matter Nucl. Sci. 15, p 81 (2015);
- [37] Swartz, M. R, Peter L. Hagelstein, Increased PdD anti-Stokes Peaks are Correlated with Excess Heat Mode, J. Condensed Matter Nucl. Sci. 24, 130-145 (2017)
- [38] Swartz, M. R, Increase of an Anti-Stokes Peak at the Cathode of an Electrically Driven, Active Aqueous Nickel/H₂O/Pt System, J. Condensed Matter Nucl. Sci., Vol 279, 22 (2018)
- [39] Swartz, M.R. “Optical Detection of Phonon Gain Distinguishes an Active Cold Fusion/LANR Component”, JCMNS, 20, 29-53 (2016)
- [40] Swartz, M. R, Active LANR Systems Emit a 327.37 MHz Maser Line, Proc. ICCF-22, J. Condensed Matter Nucl. Sci., Volume 33, pages 80-110 (2020)
- [41] Swartz, M. R, FCC Vacancies in ZrO₂PdD RF are the Active LANR Site, Proc. ICCF-22, J. Cond.Matter Nucl. Sci., Volume 33, pages 126-144 (2020)
- [42] Swartz, M. R, Pulsatile Superhyperfine Lines at 327.37 MHz Herald LANR Activity and Possible Mass-Energy Transfer, Proc. ICCF-22, J. Condensed Matter Nucl. Sci. , Volume 33, pages 111-125 (2020)
- [43] Fleischmann M., S. Pons, “Electrochemically Induced Nuclear Fusion of Deuterium”, J. Electroanal. Chem., 261 [erratum, 263, 187] (1989) 301-308
- [44] Fleischmann M., S. Pons, “Some comments on the paper Analysis of Experiments on Calorimetry of LiOD/D₂O Electrochemical Cells, R.H.Wilson et al., J. Electroanal. Chem., 332 (1992) 1* “, J. Electroanal. Chem., 332, (1992) 33-53
- [45] Fleischmann M., S. Pons, M. Anderson, L.J. Li, M. Hawkins, “Calorimetry of the palladium-deuterium-heavy water System”, Electroanal. Chem., 287, (1990) 293
- [46] Fleischmann M., S. Pons, “Calorimetry of the Pd-D₂O system: from simplicity via complications to simplicity”, Physics Letters A, 176, (1993) 118-129
- [47] McKubre MCH, Crouch-Baker S, Rocha-Filho RC, Smedley SI, Tanzella FL, Passell TO, Santucci J, “Isothermal flow calorimetric investigations of the DIPd and H/Pd systems”, J. Electroanal. Chem. 368 (1994) 55.
- [48] Cravens, Dennis, “Flowing Electrolyte Calorimetry”, Proceedings of 5th International Conference on Cold Fusion, 79-86 (1995).
- [49] Swartz M. Thermal Conduction and Non-Differential Temperature Corrections to the Enthalpic Flow Equation, J. New Energy 3, No. 1, (1998), p 10-13; www.iscmns.org/FIC/J/JNE3N1.pdf
- [50] Melcher, James “Continuum Electromechanics,” MIT Press, Cambridge, 10. 13-10. 18 (1981). https://www.google.com/url?sa=t&rct=j&q=&esrc=s&source=web&cd=4&cad=rja&uact=8&ved=2ahUKEwj8pc7XrIjjAhVorlkKHfQjBI4QFjADegQIBhAC&url=https%3A%2F%2Focw.mit.edu%2Fans7870%2Fresources%2Fmelcher%2Fresized%2Fcem_811.pdf&usq=AOVawVawIityC4BWIIPTM792pP5DX7

- [51] Chandrasekhar, S., “Hydrodynamic and Hydromagnetic Stability,” Clarendon Press. Oxford, 9-75 (1961).
- [52] Swartz, M. R., “Potential for Positional Variation in Flow Calorimetric Systems”, *Journal of New Energy*, 1, 1, 126-129 (1996) [http://world.std.com/~mica/Swartz_Calib-ErrorsbyVerticalFlow\(1996\).pdf](http://world.std.com/~mica/Swartz_Calib-ErrorsbyVerticalFlow(1996).pdf)
- [53] Swartz, M. R., “Heat Transported by Buoyant force May Augment solution convection in Flow calorimetric systems”, “Sixth International Conference on Cold Fusion”, October 1996, Toya, Hokkaido, Japan (1996). http://world.std.com/~mica/Swartz_Calib-HeatBouyantForce.pdf
- [54] Swartz, M. R., “Linear Correction for Heat Transport Secondary to Buoyant Forces in Flow Calorimetric Calculations”, (1996). [http://world.std.com/~mica/Swartz-Calib-LinearCorrxn\(1996\).pdf](http://world.std.com/~mica/Swartz-Calib-LinearCorrxn(1996).pdf)
- [55] Swartz, M. R., “Improved Calculations Involving Energy Release Using a Buoyancy Transport Correction”, *Journal of New Energy*, 1, 3, 219-221 (1996). [http://world.std.com/~mica/Swartz-Calib-ImprovCalc\(1996\).pdf](http://world.std.com/~mica/Swartz-Calib-ImprovCalc(1996).pdf)
- [56] Swartz, M. R. Buoyant Heat Transport in Flow Calorimetry, *Proc. ICCF-22, J. Condensed Matter Nucl. Sci.*, Volume 33, pages (2020); [18] Jacques Ruer, Basics of air flow calorimetry, paper n58, 22nd International Conference for Condensed Matter Nuclear Science ICCF-22 (2019).
- [57] Nicolas Léonard Sadi Carnot; https://en.wikipedia.org/wiki/Nicolas_Léonard_Sadi_Carnot
- [58] Carnot, Sadi (1977), Mendoza, E. (ed.), *Reflection on the Motive Power of Fire and other papers translated into English*, Gloucester, Massachusetts Peter Smith Wilson, S.S.(August 1981), “Sadi Carnot”, *Scientific American*, 245 (2): 102-114, 1981 doi:10.1038/scientificamerican0881-134
- [59] June 12, 1824: Sadi Carnot publishes treatise on heat engines, *This Month in Physics History*, APS News, June 2009 (Volume 18, Number 6) <https://www.aps.org/publications/apsnews/200906/physicshistory.cfm>
- [60] S A Ulybin, The founder of the theory of heat : Bicentenary of S Carnot’s birth (Russian), *Vestnik Ross. Akad. Nauk* 66 (6) (1996), 518-521.
- [61] F Sebastiani, The caloric theories of Laplace, Poisson, Sadi Carnot and Clapeyron, and the theory of thermal phenomena in gases formulated by Clausius in 1850 (Italian), *Physis-Riv. Internaz. Storia Sci.* 23 (3) (1981), 397-438.
- [62] T.S.Kuhn, Engineering precedent for the work of Sadi Carnot, *Archives internationales d’histoire des sciences* 13 (1960), 251-255.
- [63] Harald Sack, Nicolas Léonard Sadi Carnot (1796-1832), *physics* 1, June 2020 <http://scihi.org/carnot-thermodynamics/>
- [64] C. E. Shannon, “Prediction and Entropy of Printed English,” *Bell Systems Technical Journal*, 30, 1951 pp. 50-64. www.ics.uci.edu/~fowlkes/class/cs177/shannon_51.pdf.
- [65] Evaluation Metrics for Language Modeling 18.Oct. 2019 file:///C:/Users/Public/Documents/Evaluation%20Metrics%20for%20Language%20Modeling.htm
- [66] Walther Nernst, Walther Hermann Nernst; <https://www.britannica.com/biography/Walther-Nernst> https://en.wikipedia.org/wiki/Walther_Nernst; Walther Nernst;
- [67] Cherwell, F. Simon (1942). “Walther Nernst, 1864-1941”. *Obit. Note. Fell. R. Soc. Lond.* 4 (11): 1022.
- [68] Mendelssohn, Kurt Alfred Georg (1973), *The World of Walther Nernst: The Rise and Fall of German Science*. London: Macmillan. ISBN 978-0-333-14895-2; Mendelssohn, K. (1973), *The World of Walther Nernst*, University of Pittsburgh Press. p. 39. ISBN 978-0-8229-1109-8;
- [69] Barkan, Diana Kormos (1998). *Walther Nernst and the Transition to Modern Physical Science*. Cambridge: Cambridge University Press. ISBN 978-0-521-44456-9.
- [70] H. H. Uhlig, “Corrosion and Corrosion Control”, Wiley (1971).
- [71] J. O’M Bockris, A. K. N. Reddy, “Modern Electrochemistry”, Plenum Press (1970).
- [72] Swartz, M. R, Water Is Best, *Infinite Energy*, 134, pp 16-29, July/August (2017)
- [73] Swartz, M., “Dances with Protons - Ferroelectric Inscriptions in Water/Ice Relevant to Cold Fusion and Some Energy Systems”, *Infinite Energy*, 44, (2002).
- [74] von Hippel, A., Knoll, D.B., and Westphal, W.B. 1971. “Transfer of Protons Through ‘Pure’ Ice Ih Single Crystals,” *J. Chem. Phys.*, 54, 134.
- [75] von Hippel, A. and Farrell, E.E 1973. *Mat. Res. Bull.*, 8,127. von Hippel, A. “Molecular Mechanisms of Conduction and Polarization in Water Vapor, Liquid Water, and Ice, MIT 1972-1973.
- [76] von Hippel, A. 1971. *J Chem. Phys.*, 54, 145.
- [77] Bjerrum, N. 1951. *Kgl. Danske Videnskab. Selskab., Fys. Medd.*, 27,1.
- [78] Bjerrum, N. 1951. *Dansk. Mat.-Fys. Medd.*, 27, 32. Bjerrum, N. 1951. *Dansk. Mat.Fys. Medd.*, 27, 41.



Research Article

The Use of Graphene for Controlled LENR in Thin Conductive Targets via Optimized Low-Voltage Corona Discharge

V. I. Vysotskii and M. V. Vysotskyy

Taras Shevchenko National University of Kyiv, Kyiv, Ukraine

S. Bartalucci

INFN - Laboratori Nazionali di Frascati, Frascati, Italy

Abstract

The problem of optimizing nuclear reactions at low energy of moving particle based on accelerator nuclear fusion is considered. It is shown that the optimization process may be linked to the formation of coherent correlated states of moving particles and accompanying fluctuations of transverse energy (30–100 keV). These phenomena occur when particles traverse a crystalline graphene channel (graphene nanotube) with an optimal energy of longitudinal motion around 500 eV. Furthermore, the study establishes that the most efficient method for implementing such systems is the use of a negative corona discharge in hydrogen or deuterium gas near the surface of conductive graphene nanotubes, in the presence of lithium or other fusion-optimal isotopes inside these nanotubes.

© 2025 ICCF. All rights reserved. ISSN 2227-3123

Keywords: Graphene nanotubes, Coherent correlated state, Low energy nuclear reactions, Corona discharge, Nuclear fusion

1. Introduction

Traditional “accelerator nuclear fusion” methods rely on the need to use high kinetic energy particles that interact with remote unoriented targets possessing optimal isotopic composition for fusion. The efficiency of such fusion remains quite low (3...5%) due to the substantial non-nuclear deceleration of moving particles upon interaction with atomic electrons of the target [1]. While employing the channeling motion of accelerated particles in oriented crystal targets significantly reduces the rate of non-nuclear deceleration, the probability of nuclear fusion decreases even more rapidly. Such interaction modes necessitate intricate and costly accelerator systems. It has been shown that the combination of these methods using thin layers of graphene leads to the possibility of a simple alternative implementation of low-energy, self-sustaining and self-regulating fusion.

2. Application of Coherent Correlated State of Moving Particles for LENR

In our previous investigations [2]–[5], we have demonstrated the feasibility of accelerator $p + Li^7 = 2He^4$ fusion utilizing moving protons with an optimal low velocity $v_{z,opt} = 2d < \omega(z) >$ and low kinetic energy $E_{z,opt} =$

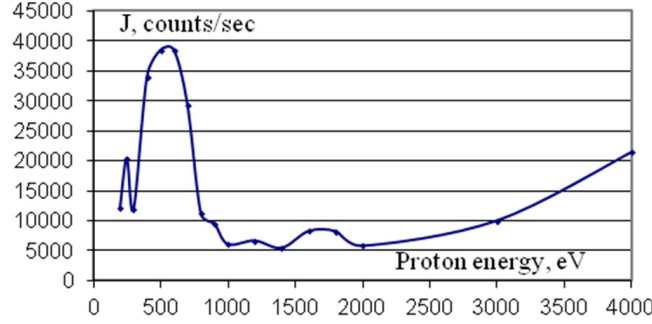


Figure 1. Dependence of the intensity of $Li^7(p, \alpha)He^4$ fusion reaction versus proton energy E_z [6].

$Mv_{z,opt}^2/2 \approx 500\text{eV}$, corresponding to longitudinal motion within the periodic interplanar potential

$$V(r_{\perp}, r_{\parallel}) = V(r_{\perp}, r_{\parallel} + nd) = M\{\omega(z)\}^2 x^2/2, \quad r_{\perp} = x, r_{\parallel} = z \quad (1)$$

of Li crystal. These conditions align well with the experimental data [6] (see Fig. 1) and correspond to the formation of a coherent correlated state (CCS) of the moving particle upon traversing a crystalline channel [2]–[5].

It should also be noted that the optimal energy $E_{z,opt}$ for different isotopes of the same chemical element (e.g., p and d) will be identical. This follows directly from the formulas for $v_{z,opt}$ and $E_{z,opt}$, taking into account that for different isotopes $\omega(z) \sim 1/M^{1/2}$.

This CCS is characterized by significant fluctuations δE_x in transverse energy at low energy T_{opt} of longitudinal motion, leading to subsequent fusion within the volume of the same Li crystal. This process is associated with the formation of an optimal coherent superposition of eigenfunctions of each particle, satisfying the criteria for realizing Schrödinger-Robertson uncertainty relations for various pairs of dynamic variables (e.g., p_x, x and E_x, t [2]–[4], [7]–[22]):

$$\begin{aligned} \delta p_x \delta x &\geq \frac{\hbar}{2\sqrt{1-r_{p_x x}^2}} \equiv G_{p_x t} \hbar/2 \equiv \hbar_{\text{eff}}/2, \quad \delta E_x \delta t \geq \frac{\hbar}{2\sqrt{1-r_{E_x t}^2}} \equiv G_{E_x t} \hbar/2 \equiv \hbar_{\text{eff}}/2, \quad (2) \\ r_{p_x x} &= \frac{\{\langle x p_x \rangle + \langle p_x x \rangle\}}{2\sqrt{\langle p_x^2 \rangle \langle x^2 \rangle}}; \quad r_{E_x t} = \frac{\{\langle t E_x \rangle + \langle E_x t \rangle\}}{2\sqrt{\langle E_x^2 \rangle \langle t^2 \rangle}}; \\ G &= 1/\sqrt{1-r^2}; \quad 0 \leq |r| < 1; \quad 1 \leq G < \infty. \end{aligned}$$

Here r is the coefficient of correlation, and G is the coefficient of correlation efficiency, characterizing the increase in amplitudes of dynamic variables fluctuations. It is noteworthy that during the formation of a coherent correlated state based on, for example, an excited oscillator, the Schrödinger-Robertson uncertainty relation is an obvious generalization of (2) and takes the form [10], [11]

$$(\delta p_x)^2 (\delta x)^2 \geq G^2 (2n+1) \hbar^2 / 4. \quad (3)$$

The value n corresponds to the number of the energy level in the transverse potential well, associated with the transverse energy of the particle upon entering the interatomic channel. From these equations, a simple estimate for the lower limit (minimum value) of the kinetic energy fluctuation of a particle with mass M localized within the spatial interval δq_{\perp} can be derived:

$$\delta E_{\perp}^{(\min)} = (\delta p_{\perp})^2 / 2M = G^2 (2n+1) \hbar^2 / 8M (\delta q_{\perp})^2 \quad (4)$$

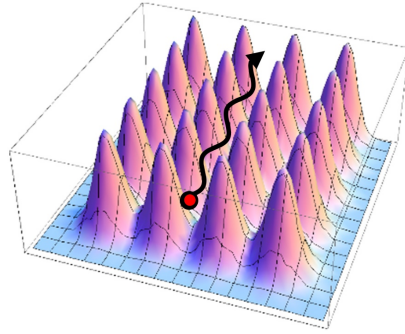


Figure 2. Adaptive channeling of low-energy proton in 3D crystal.

In particular, when a moving proton with mass M is localized in an interatomic region with size about 1.5\AA ($\delta q_{\perp} \leq 0.75\text{\AA}$), typical for condensed matter, the minimum fluctuation of kinetic energy for a particle in CCS with realistic coefficient of correlation efficiency $G = (1\dots3) \cdot 10^3$ corresponds to the value $\delta E_{\perp}^{(\min)} \approx (1\dots10) \cdot (2n + 1) \text{ keV}$. Actual fluctuations δE of transverse kinetic energy (2) can significantly exceed this minimum value $\delta E_{\perp}^{(\min)}$.

Notably, these fluctuations exhibit a considerably extended duration δt [21], [22] compared to the duration of quantum fluctuations associated with the conventional Heisenberg uncertainty relation $\delta E_{\perp} \delta t \geq \hbar/2$ for uncorrelated states with $r = 0$. The emergence of such states is linked to the physical mechanism of the formation of a mutually phased coherent superposition of particle eigenfunctions inside a nonstationary potential well. This potential well corresponds to the particle's state in the comoving coordinate system, linked to the moving particle within the periodic field of the interplanar channel of the crystal. This state corresponds to adaptive channeling within the actual periodic transverse electric field of the crystal (Fig. 2).

At the proton kinetic energy $E_{z,\text{opt}} = Mv_{z,\text{opt}}^2/2$, the coefficient of correlation efficiency increased up to $G_{\text{max}} \approx (2\dots3) \cdot 10^4$ over three lattice periods [2]–[4]. This augmentation results in substantial fluctuations in transverse kinetic energy $\delta E_{\perp} \geq 30\dots100 \text{ keV}$ and a pronounced increase in the transparency of the Coulomb barrier from an initial small value $D(E_{z,\text{opt}}) \leq 10^{-80}$ to $D(\delta E_{\perp}) \approx 0.01$.

A comparable, albeit less intense, effect transpires when a charged particle traverses a single lattice period, as may occur when a particle moves through a single-layer crystalline film of the graphene type (Fig. 3).

The motion of a proton through a unit cell of a single-layer graphene corresponds to a two-dimensional nonstationary harmonic oscillator with similar Schrödinger-Robertson uncertainty relations (1) for the corresponding variables p_x, x and E_x, t . The results of the numerical calculation of CCS for a single-layer graphene [2]–[4] are shown in Fig. 4.

These calculations demonstrate that the optimal particle velocity giving the maximum correlation coefficients corresponds to the energy $E_{z,\text{opt}} \approx 500 \text{ eV}$ of longitudinal motion.

3. LENR on Targets Connected With Graphene Nanotubes During Corona Discharge In H or D Gas

The practical realization of this straightforward method for stimulating LENR can be achieved through two alternative approaches:

- utilizing a high-current proton accelerator with specific energy in vacuum system;
- employing the method of directed accelerating ions in a dense gaseous environment across the entire space between two electrodes with an optimal potential difference.

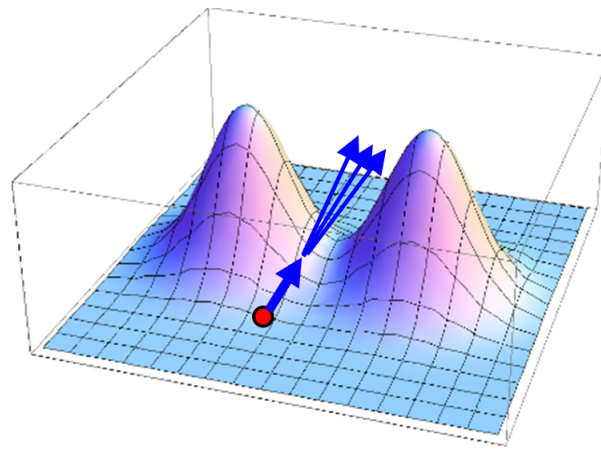


Figure 3. Adaptive channeling of protons in a single-layer crystalline film.

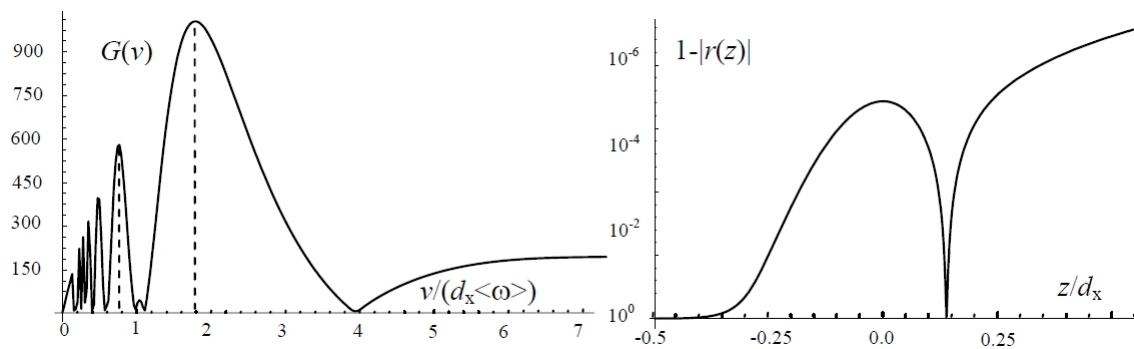


Figure 4. Dependence of the coefficients r and G on the velocity $v = v_z$ in the center of the longitudinal potential well of single-layer graphene with width d_x (left) and on the longitudinal coordinate z at the optimal longitudinal velocity $v_{z,opt}$ of the particle (right).

The first method demands specialized and rather intricate systems. Conversely, the second method faces challenges in maintaining a constant speed of protons due to multiple collisions between accelerated ions and other ions and atoms within the gaseous medium.

Simultaneous fulfilment of the conditions necessary for CCS creation and LENR realization (formation of quasi-monochromatic beams of particles with optimal energy and ensuring the optimal direction of their movement) can be attained by employing conductive single-walled graphene nanotubes and employing a corona discharge mode at the applied voltage U in a gaseous environment with an optimal isotopic composition.

It is well known that the primary characteristic of a corona discharge is the acceleration of positively charged ions occurring directly near the cathode surface with a small radius R . In this region, a very high radial electric field strength

$$E_r = U/r \ln(r/R), \quad r \geq R \tag{5}$$

is present and a maximum rate of ion acceleration towards the surface of cylindrical cathode is realized.

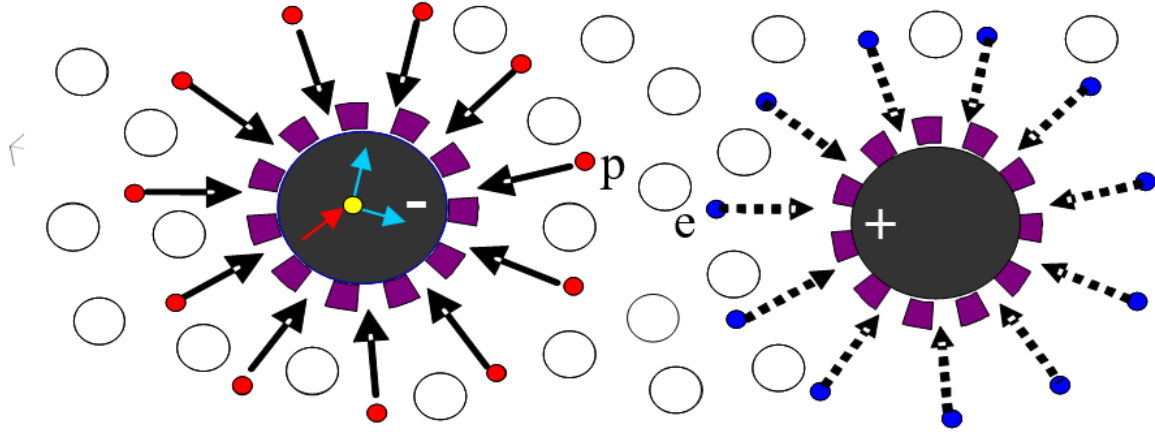


Figure 5. Setup scheme for CCS formation and LENR stimulation during negative corona p (or d) discharge near thin fusion active wires with optimal isotopic composition (e.g. Li), coated with single-layer conducting graphene tubes. Left: motion of protons or deuterons near wire cathode; right: motion of electrons near wire anode.

The schematic of a setup that meets all these requirements and can be used to implement nuclear fusion inside a target is shown in Fig. 5.

This system utilizes cathodes and anodes in the form of thin conductive wires with a small radius and optimal isotope composition for fusion (e.g., Li). They are coated with single-layer graphene tubes to enable a negative corona discharge mode.

The automatic provision of these conditions is associated with the features of the corona discharge near the surface of a cylindrical cathode with radius R . When the conditions for the existence of such a discharge are met, the entire process of ion acceleration occurs within a limited space interval $\Delta r \leq 10R$ near the cathode surface. The diminutive size of the acceleration path Δr for corona discharge results in a substantial suppression of the process of scattering and deceleration of accelerated ions by other ions or gas atoms. This is attributed to the fact that the average path length of the accelerated ion $\langle l \rangle = 1/\sigma_{scat}n_{a,i}$ is significantly greater than the size Δr of the ion acceleration region near the cathode surface composed of a graphene nanotube. Moreover, the movement of accelerated particles transpires in a direction perpendicular to the surface of a thin cylindrical cathode, ensuring the necessary orientation of particle movement. These conditions automatically ensure a high degree of monochromaticity for accelerated particles in a gas medium with an atom or heavy-ion concentration $n_{a,i} < 1/(10\sigma_{scat}R)$. In particular, at $R = 1\text{--}100\text{ nm}$ and a typical value of $\sigma_{scat} = 10^{-16}\text{ cm}^2$, we obtain the critical condition $n_{a,i} < 10^{23}\text{--}10^{21}\text{ cm}^{-3}$.

In this setup, the initial acceleration of particles (p or d) to the optimal energy $E_{r,opt} \approx eU$ transpires radially within a small region near the cathode wires. As particles possessing the optimal energy traverse through a monocrystalline graphene film in a short-range channeling regime, a CCS of these particles is formed [2]–[4].

An important fact is that in close proximity to the surface of a graphene nanotube, the direction of the accelerated particles will typically deviate slightly from the strictly radial direction. This results in the occupation of quantum states with $n \geq 3 - 5$ within the space between graphene atoms and, consequently (as per equation (4)), an increase in transverse energy fluctuation $\delta E_{\perp} \sim (2n + 1)$ up to 30... 100 keV and more. This angular deviation in the direction of movement arises from the influence of the electric field immediately before the particle enters the space between atoms on the graphene surface.

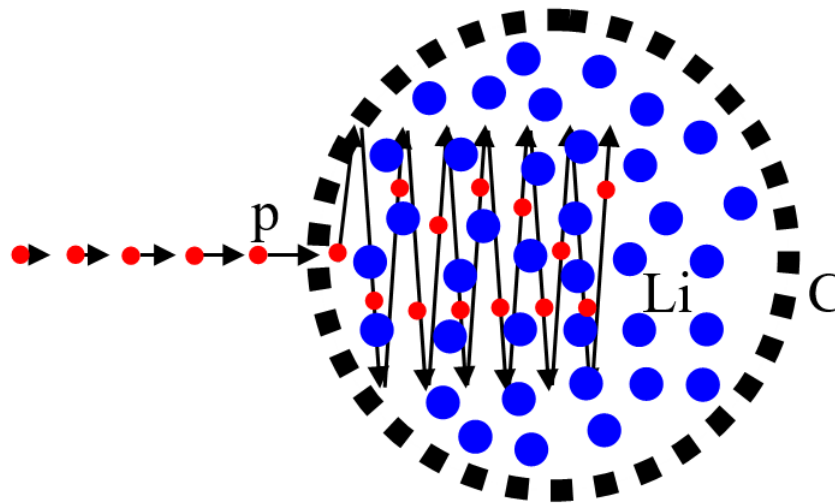


Figure 6. Schematic diagram of the motion of a proton with the optimal initial radial energy $E_{r,opt}$ and large transverse energy fluctuations δE_{\perp} in the presence of CCS inside a nanotube filled with unstructured lithium.

The interaction of these particles in CCS with an adjacent unstructured *Li* cathode, proximate to the film, leads to effective $Li^7 + p = 2He^4$ nuclear fusion (see Fig. 6).

This corona discharge mode, with a voltage of $U \approx 450...500 V$, can persist (in accordance with Peek's law [23], [24]) for an extended duration within hydrogen gas with a concentration up to $n_a \approx 10^{20}...10^{21} cm^{-3}$ at $R \approx 1...10 nm$. For cathode surface self-cleaning and removal of space charge near the cathode surface, it is imperative to periodically interchange the anode and cathode by changing the voltage U polarity.

An important factor in implementing this self-acceleration method is the energy loss that accelerated ions experience while passing through the surface of the graphene nanotube.

This issue is addressed in [25]. The authors conducted a detailed theoretical and experimental study of the parameters of such losses in the case of an oriented proton beam moving perpendicular to the surface of single-layer graphene. They showed that in this mode of motion, the energy loss increases linearly with the velocity of the incident particle. This finding is in good agreement with the Lindhard–Scharf theory of electronic stopping [26]. In particular, for single-layer graphene, the energy loss for protons with an energy of $500 eV$ is about $10 eV$, which does not significantly affect the efficiency of nuclear fusion.

4. Conclusions

The method of self-controlled formation of coherent correlated states of particles passing through an optimal single- or double-layer graphene-type nanotubes enables the generation of giant fluctuations in transverse momentum and energy. The optimal longitudinal energy for protons or deuteron is in the range of $450...500 eV$. Such fluctuations are generated and exist not only during particle passage through a thin graphene surface, but also in the space beyond this surface (inside the graphene nanotube [20]). The most optimal approach to creating such a system with controlled particle energy is through a corona electric discharge in hydrogen or deuterium gas, involving conducting graphene nanotubes as both cathode and anode.

This configuration involves the interaction of protons accelerated to the optimal for CCS energy E_{opt} with an unstructured fusion-active target (e.g., $p + Li^7 = 2He^4$) made of *Li*-type isotope material. This target is situated inside the conducting nanotube.

The use of nanotubes with different internal isotopic compositions allows a significant increase in the number of nuclear fusion reaction types, facilitating the search for the most optimal configurations. When empty graphene nanotubes are used, only a single optimal reaction $C^{12} + d = N^{14}$ can be implemented via the direct interaction of accelerated deuterons with the nanotube wall [27].

It is particularly important that the feasibility and high efficiency of implementing a corona discharge in a graphene nanotube system have been confirmed in successful experiments [28], [29]. These experiments did not involve nuclear physics studies but demonstrated the high efficiency of this electric discharge mode.

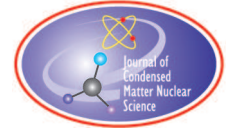
Another challenge in implementing such LENR technology concerns the formation of complex targets consisting of a graphene nanotube containing an isotope optimal for this fusion. At first glance, introducing such a nuclear-active core into a very thin graphene nanotube appears to be a highly complex and expensive technological task.

In practice, however, similar problems have already been successfully solved in applied electronics. One approach involves first forming thin nanowires from an optimal conductive material enriched with the required isotope using the electrospinning method, followed by a corona discharge in an atmosphere containing carbon. This process results in the deposition of a thin carbon layer in the form of graphene on the nanowire surface [30]. Another method for forming such systems involves introducing lithium into an existing graphene nanotube with a diameter of 1.5–5 nm via the thermocapillary effect at temperatures above 200°C [31].

References

- [1] V.I.Vysotskii, M.V.Vysotskyy, S.Bartalucci. Nuclear fusion in ordered crystal targets bombarded by monochromatic beams of light or middle-mass isotopes. *Ann. Nucl. Energy*, **62** (2013), 613.
- [2] V.I.Vysotskii, M.V.Vysotskyy, S.Bartalucci. Features of the formation of correlated coherent states and nuclear fusion induced by the interaction of slow particles with crystals and free molecules. *J. Exper. Theor. Phys. (JETP)*, 127(3) (2018), 479–490.
- [3] V.I.Vysotskii, M.V.Vysotskyy, S. Bartalucci. Using the method of coherent correlated states for production of nuclear interaction of slow particles with crystals and molecules. *J. Condensed Matter Nucl. Science*, **29** (2019), 358–367.
- [4] S.Bartalucci, V.I.Vysotskii, M.V.Vysotskyy. Correlated states and nuclear reactions: An experimental test with low energy beams. *Phys. Rev. AB*, **22** (2019) 054503.
- [5] S.Lipinski, H.Lipinski, Hydrogen-lithium fusion device, Patent No.WO 2014/189799 A9, 2013.
- [6] V.I.Vysotskii, M.V.Vysotskyy. Application of correlated wave packets for stimulation of LENR in remote targets. *J. Condensed Matter Nucl. Science*, **33** (2020), 305–313.
- [7] E.Schrödinger. Heisenbergschen Unschärfepinzip. *Ber. Kgl. Akad. Wiss., Berlin*, **S24** (1930) 296.
- [8] H.P.Robertson, A general formulation of the uncertainty principle and its classical interpretation, *Phys. Rev. A*, **35**, (1930), 667.
- [9] V.V.Dodonov, E.V.Kurmishev, V.I. Manko, Generalized uncertainty relation and correlated coherent states, *Phys. Lett. A*, **79** (1980), 150.
- [10] V.V.Dodonov, V.I.Manko. Invariants and correlated states of nonstationary systems, in: Invariants and the evolution of nonstationary quantum systems, Nova Science, Commack, New York, 183 (1988) 103–261.
- [11] V.V.Dodonov, A.B.Klimov, V.I. Manko. Physical effects in correlated quantum states in squeezed and correlated states of quantum systems, Nova Science, Commack, New York, **295** (1993) 61.
- [12] V.I.Vysotskii, S.V.Adamenko, Correlated states of interacting particles and problems of the coulomb barrier transparency at low energies in nonstationary systems. *J. Tech. Phys.* **55**, (2010), 613–621.
- [13] V.I.Vysotskii, M.V. Vysotskyy, S.V. Adamenko, Formation and application of correlated states in non-stationary systems at low energy of interacting particles. *J. Exper. Theor. Phys.* **114**(2) (2012), 243.

- [14] V.I.Vysotskii, S.V.Adamenko, M.V. Vysotskyy, The formation of correlated states and the increase in barrier transparency at a low particle energy in nonstationary systems with damping and fluctuations. *J. Exp. Theor. Phys.* **115**(4) (2012), 551.
- [15] V.I.Vysotskii, S.V.Adamenko, M.V. Vysotskyy, Subbarrier interaction of channeling particles under the self-similar excitation correlated states in periodically deformed crystal. *Journal of surface investigation*, **6**(2) (2012), 369.
- [16] V.I.Vysotskii, M.V. Vysotskyy, Coherent correlated states and low-energy nuclear reactions in non stationary systems. *European Phys. Jour: A*, **49** (2013), 99.
- [17] V.I.Vysotskii, S.V.Adamenko, M.V. Vysotskyy, Acceleration of low energy nuclear reactions by formation of correlated states of interacting particles in dynamical systems. *Annals of Nuclear energy*, **62** (2013), 618.
- [18] V.I.Vysotskii, M.V. Vysotskyy, Correlated states and transparency of a barrier for low-energy particles at monotonic deformation of a potential well with dissipation and a stochastic force. *J. Exp. Theor. Phys.* **118**(4) (2014), 534.
- [19] V.I.Vysotskii, M.V.Vysotskyy, Correlated states and transparency of a barrier for low-energy particles at monotonic deformation of a potential well with dissipation and a stochastic force. *Current Science*, **108** (2015), 524.
- [20] V.I.Vysotskii, M.V. Vysotskyy. Application of correlated wave packets for stimulation of LENR in remote targets, *Journal Condensed Matter Nucl. Science*, **33** (2020), 305–313.
- [21] V.I.Vysotskii, M.V.Vysotskyy, Features of correlated states and a mechanism of self-similar selection of nuclear reaction channels involving low-energy charged particles, *J. Exp. Theor. Phys.* **128** (2019), 856–864.
- [22] V.I.Vysotskii, M.V.Vysotskyy. Universal mechanism of LENR in physical and biological systems on the base of coherent correlated states of interacting particles. *Cold Fusion. Advances in Condensed Matter Nuclear Science*, Edited by Jean-Paul Biberian. Elsevier, 2020. CHAPTER 17, pp. 333–370.
- [23] E.Kuffel, W.S.Zaengl and J.Kuffel. *High voltage engineering fundamentals*. Butterworth-Heinemann, 2000.
- [24] Morgan J. Hurley, Daniel T.Gottuk and John R. Hall, Jr. *SFPE Handbook of fire protection engineering*. Springer, 2015.
- [25] Anna Niggas, Lukas Fischer, Silvan Kretschmer, Matthias Werl, Herbert Biber, Carsten Speckmann, Niall McEvoy, Jani Kotakoski, Friedrich Aumayr *et al.* Charge-exchange-dependent energy loss of H and He in freestanding monolayers of graphene and MoS₂. *Phys. Rev. A* **108** (2023), 823. doi: <https://doi.org/10.1103/PhysRevA.108.062823>.
- [26] J.Lindhard, M.Scharff, Energy dissipation by ions in the kev region, *Phys. Rev.* **124** (1961), 128.
- [27] V.I.Vysotskii, M.V.Vysotskyy, S. Bartalucci. Unlimited-time nuclear fusion via self-controlled periodic d(p) channeling in empty nanotubes under corona discharge. *Nuclear Instruments and Methods in Physics Research A*, 1075 (2025) 170402.
- [28] R. Rosen, W. Simendinger, C. Debbault, H. Shimoda, L. Fleming, B. Stoner and O. Zhou. Application of carbon nanotubes as electrodes in gas discharge tubes. *Applied Physics Letters* **76**, Number 13 (2000), 1668–1670.
- [29] Lili Wu, Aiyang Lin, Baiji Lu et al. Experimental study of corona discharge with multi-walled carbon nanotubes electrode. Proceedings of the 2009 Intern. Conf. IEEE on Robotics and Biomimetics. doi:10.1109/ROBIO.2009.5420486
- [30] Ming-we Li i, Zheng Hu, Xi-zhang Wang, Qiang Wu, Yi Chen, Yi-Ling Tian. Low-temperature synthesis of carbon nanotubes using corona discharge plasma at atmospheric pressure. *Diamond & Related Materials*, **13** (1),(2004) 111–115. doi:10.1016/j.diamond.2003.09.008
- [31] Chanda, D., Shigeta, K., Gupta, S. *et al.* Large-area flexible 3D optical negative index metamaterial formed by nanotransfer printing. *Nature Nanotech.* **6** (2011), 402–407. <https://doi.org/10.1038/nnano.2011.82>



Research Article

Stimulation of Efficient Low Energy Tritium Fusion Under The Action of a Weak Undamped Thermal Wave on Remote TiD Target

Vladimir I. Vysotskii

Taras Shevchenko National University of Kyiv, Ukraine

Alla A. Kornilova

Member of Condensed Matter Nuclear Science Society, AVSystems Inc., 54, Harpsichord TPKE, Stamford, USA

Sergey N. Gaydamaka

AVSystems Inc., 54, Harpsichord TPKE, Stamford, USA

Abstract

This study investigates the implementation of (dd) low-energy nuclear reactions (LENR) under the influence of an undamped weak thermal (temperature) wave on a remote *TiD* target. These waves are generated in the air during the cavitation of a water jet in a closed chamber. The research reveals that the rate of tritium fusion is approximately 10^8 times greater than the rate of helium fusion in these (dd) reactions.

© 2025 ICCF. All rights reserved. ISSN 2227-3123

Keywords: Undamped thermal waves, Coherent correlated states, Low energy nuclear reactions

1. Introduction

It is widely acknowledged that current methods and projects aimed at achieving nuclear fusion are fraught with significant technological challenges. This paper explores a potential mechanism for stimulating LENR involving the generation, propagation, and distant influence of thermal waves. Contrary to the conventional understanding that such waves rapidly dampen, transforming into an unstructured thermal field, our investigation challenges this notion. The classical thermodynamic perspective assumes that the non-equilibrium system under study can be represented as numerous small local equilibrium subsystems. The mathematical description of this process relies on the simultaneous application of two fundamental equations:

the Fourier law for nonstationary heat flux $\vec{q}(\vec{r}, t)$

$$\vec{q}(\vec{r}, t) = -\lambda \cdot \text{grad}(T(\vec{r}, t)) \quad (1)$$

and the equation of continuity

$$\rho c_v \frac{\partial T(\vec{r}, t)}{\partial t} = \text{div} \vec{q}(\vec{r}, t). \quad (2)$$

Here λ , ρ and c_v are coefficients of heat transfer, density, and specific heat.

From (1) and (2) follows the usual wave equation for the temperature field and thermal waves

$$\rho c_v \frac{\partial T(\vec{r}, t)}{\partial t} = \text{div} \{ \lambda \text{grad}[T(\vec{r}, t)] \}. \quad (3)$$

The solutions of this equation in 1D case are two colliding plane thermal (temperature) waves

$$T(\omega, x, t) = A_\omega e^{-\kappa x} e^{i(\omega t - \kappa x)} + B_\omega e^{\kappa x} e^{i(\omega t + \kappa x)} \quad (4)$$

with a significant damping coefficient equal to the wave number κ :

$$\delta \equiv \kappa = \sqrt{\omega/2G}. \quad (5)$$

Here $G = \lambda/\rho c_v$ is a coefficient of thermal diffusivity.

Notably, the conventional “standard” thermal wave (4) demonstrates attenuation over a spatial distance equivalent to the wavelength, and we have $\delta \approx 10^4 \text{ cm}^{-1}$ and attenuation length of $\delta^{-1} \approx 1 \text{ }\mu\text{m}$ for air at $\omega = 80 \text{ MHz}$. However, it becomes apparent that the standard classical equations of thermodynamics (1–3) were derived under inaccurate assumptions, failing to consider relaxation processes. The solution (4) for thermal waves is valid solely for low-frequency heat waves.

2. Fundamental Concepts of Undamped Thermal Waves Theory

Equations (1–3) are founded on the approximate assumption that the energy thermal flow $\vec{q}(\vec{r}, t)$ and temperature $T(\vec{r}, t)$ change synchronously within any small area along the wave propagation trajectory. This traditional yet erroneous assumption is rectified through a detailed analysis, revealing that a formal decrease in microvolume does not correspond to a decrease in relaxation time. The latter necessitates a substantial number (approximately ~ 10) of collisions between atoms and molecules. For accurate analysis, the continuity equation (1) must be modified with a time shift τ and considering the portion of the equation influenced by thermal action - whether it involves the change in temperature $T(\vec{r}, t)$ over time within the microvolume due to introduced energy

$$\text{div} \vec{q}(\vec{r}, t) \Rightarrow -\rho c_v \frac{\partial T(\vec{r}, t + \tau)}{\partial t}, \quad (6)$$

or the change in the flow $\vec{q}(\vec{r}, t)$ in space resulting from temperature changes

$$\rho c_v \frac{\partial T(\vec{r}, t - \tau)}{\partial t} \Rightarrow -\text{div} \vec{q}(\vec{r}, t). \quad (7)$$

The time shifts in both equations, determined by identical relaxation processes, can be assumed with high accuracy to be identical and equal to the thermodynamic relaxation time τ . As heat waves propagate, these processes remain interconnected, compelling the consideration of both equation variants. Consequently, a joint analysis of these equations, along with Fourier’s law (1) for nonstationary heat flow $\vec{q}(\vec{r}, t)$, yields a modified equation of thermal conductivity that incorporates the time delay (relaxation time τ) [1]–[5]:

$$\frac{\partial T(\vec{r}, t \pm \tau)}{\partial t} = G \nabla^2 T(\vec{r}, t) \quad (8)$$

The solution of the corrected equation (8) in 1D case can be presented as a superposition of colliding waves:

$$\begin{aligned} T(\omega, x, t) &= A_\omega e^{-\delta x} e^{i(\omega t - k'x)} + B_\omega e^{\delta x} e^{i(\omega t + kx)} \\ &\equiv A_\omega \exp\left(-\kappa \left| \cos \frac{\omega\tau}{2} \pm \sin \frac{\omega\tau}{2} \right| x\right) \exp\left\{i\left(\omega t - \kappa \left| \cos \frac{\omega\tau}{2} \mp \sin \frac{\omega\tau}{2} \right| x\right)\right\} \\ &\quad + B_\omega \exp\left(\kappa \left| \cos \frac{\omega\tau}{2} \pm \sin \frac{\omega\tau}{2} \right| x\right) \exp\left\{i\left(\omega t + \kappa \left| \cos \frac{\omega\tau}{2} \mp \sin \frac{\omega\tau}{2} \right| x\right)\right\}. \end{aligned} \quad (9)$$

These waves correspond to the wave number and absorption coefficient

$$k = \kappa \left| \cos(\omega\tau/2) \pm \sin(\omega\tau/2) \right|, \quad (10)$$

$$\delta = \kappa \left| \cos(\omega\tau/2) \mp \sin(\omega\tau/2) \right|, \quad \kappa = \sqrt{\omega/2G}. \quad (11)$$

Temperature waves with characteristic frequencies

$$\omega_n = (2n + 1)\pi/2\tau, \quad n = 0, 1, 2, \dots \quad (12)$$

are undamped temperature waves ($\delta = 0$) and they have wave number $\kappa_{\text{eff}} = \kappa(\omega_n)\sqrt{2}$:

$$T(\omega_n, x, t) = A_{\omega_n} \exp\left\{i\left(\omega_n t - \kappa\sqrt{2}x\right)\right\} + B_{\omega_n} \exp\left\{i\left(\omega_n t + \kappa\sqrt{2}x\right)\right\}. \quad (13)$$

The frequencies of these waves, under typical air parameters, are determined by

$$\omega_n \approx 80 \cdot (2n + 1) \text{ MHz}, \quad n = 0, 1, 2, \dots \quad (14)$$

These waves, characterized by their ability to propagate over long distances without attenuation, act effectively on distant targets. Their short wavelength results in a minimal diffraction expansion of their flow. Undamped waves are not only generated during precisely periodic heating with frequencies ω_n (12) applied to a layer of air or a surface bordering air but also during pulsed short-term heating with a duration Δt shorter than the relaxation time τ in air (during such pulses the spectrum of generated thermal waves will contain spectral components with a frequency ω_n (12)).

In our experiments, a pulsed method was employed, utilizing short shock waves generated during cavitation of a water jet emerging from a narrow channel into the closed volume of the cavitation chamber (Fig. 1). These experiments used ordinary drinking water (not distilled). In this system, cavitation was formed when a water jet exited through a steel channel with a diameter of about 2 mm into the closed chamber. The working pressure of water in this system corresponded to 150 atmospheres. The cavitation target was made from a steel plate approximately 2.5 mm thick. Thermal waves were generated by excitation or ionization and subsequent rapid decay or recombination of atoms on the outer surface of a flat cavitation target under the influence of acoustic shock waves formed by the interaction of water with cavitation bubbles with the inner surface of the target. Soft X-ray radiation with an energy of approximately $\hbar\omega_X \approx 1.5 \text{ keV}$, produced during decay or recombination, was absorbed rapidly in the air, heating it and leading to the excitation of thermal waves. The emitted X-ray radiation was effectively detected by an X-spectrometer or photographic plates near the outer surface [3]–[5].

Thermal waves were generated by excitation or ionization and subsequent rapid decay or recombination of atoms on the outer surface of a flat cavitation target under the influence of acoustic shock waves formed by the interaction of water with cavitation bubbles with the inner surface of the target.

The study of these undamped thermal waves involved their interaction, entailing rapid heating and cooling, with the surface of a piezocrystal in a remote acoustic detector. The resultant rapid temperature changes induced acoustic waves in the piezocrystal, recorded by the detector. These waves, recorded [4], [5] at distances of up to 2 m at frequencies corresponding to ω_n (12), with a maximum frequency reaching 1 GHz. The registration range was constrained by the size of the laboratory.

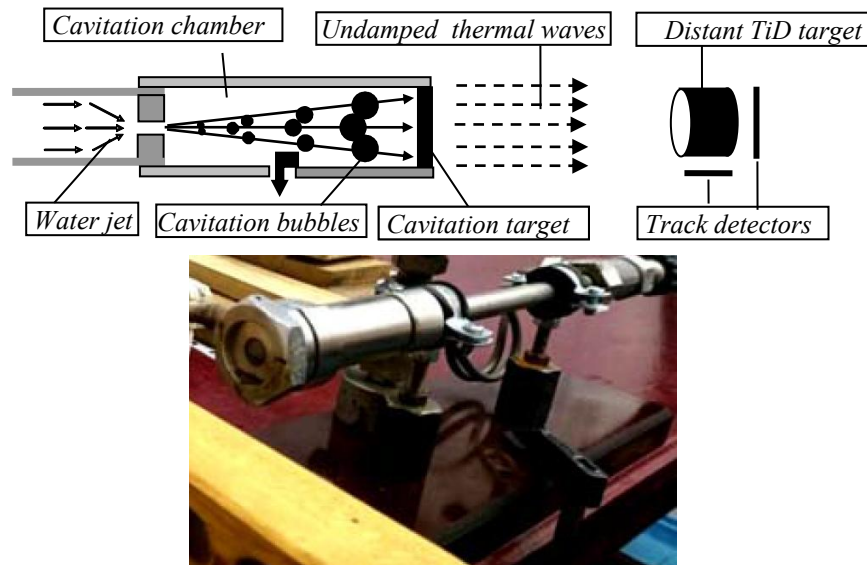


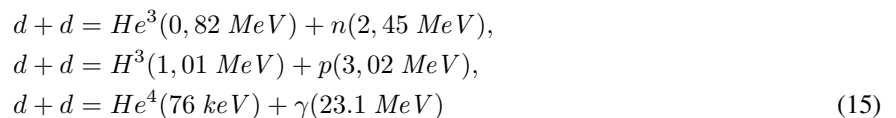
Figure 1. Scheme of experiments on the generation of undamped temperature waves and stimulation of nuclear fusion in a distant target and general view of the experimental setup.

It is necessary to take into account the structural features of the thermal wave at a relatively short distance from its source. Such a wave is a set of harmonics within the spectral interval $|\omega - \omega_n| \leq \Delta\omega$, close to optimal frequencies ω_n . These harmonics exhibited weak attenuation in air, forming a pulsed wave packet of short duration $\Delta t \approx 1/\Delta\omega$. Our calculations [1]–[5] and conducted experiments demonstrate that the action of these waves on a distant nuclear active target leads to the effective stimulation of nuclear reactions.

3. Stimulation of D-D Reactions in Distant Targets by Undamped Thermal Waves

3.1. Prerequisites of stimulating fusion by heat wave

One of the possible application of undamped thermal ways [5]–[7] is connected with direct distant stimulation of nuclear dd-fusion



The mutual redistribution of the energy of each of these reactions between the products of these reactions at low energies of their collisions corresponds to the laws of conservation of energy and momentum. Very short-term energy fluctuations associated with the uncertainty relation allow the Coulomb barrier to be overcome, but do not affect the final energy distribution among the products of these reactions.

The first two reactions correspond to the direct reaction, and in the third reaction a compound nucleus is formed. In standard thermonuclear fusion physics using really (not virtually) accelerated particles, the probabilities of the first two channels of fusion are approximately equal and the probability of the third channel of fusion (15) is very small.

For the initial deuterons, with low average real (not virtual) energy, the probability of the first reaction, with a proton being captured by a moving H^2 nucleus, is very small compared to the second reaction, due to the Oppenheimer-Phillips effect (the mutual reorientation of two interacting H^2 nuclei, resulting in the capture of a neutron and the formation of a nucleus H^3 and a free proton). At the same time, it should be recalled that the total probability of both of these reactions at low real energy will be very small due to the low probability of the tunnel effect.

For particles with high real energy, the duration of both direct reactions (in fact, the duration of the mutual counter-flight) is very small, which leads to the impossibility of mutual reorientation of these nuclei and to the same probability of the capture of a proton or neutron by a moving deuteron.

For the case of direct reactions with low average energy in the presence of a short time δt and large energy fluctuation δE , the third (alternative) option should be realized - a high probability of reaction and the fulfillment of the condition of selective neutron capture with the formation of He^3 nucleus.

For the third reaction (15) at a low average temperature of the material environment, a very low energy of the formed alpha particle is characteristic. The mean free path in air of alpha particles from the third reaction with such energy 76 keV does not exceed 0.01 cm and cannot be registered by a distant (5 mm) track detector.

For this reason, the most likely reactions observed in these experiments involve the formation of He^3 and H^3 particles. Stimulation of these reactions occurs through several successive stages. Initially, rapid temperature changes on the surface of the target result in the generation of shock waves within the target volume. These shock waves, in turn, influence the state of deuterium localized in the nanocracks of the TiD target or in the spaces between Ti atoms in the TiD lattice. The modulation of parameters of these potential wells at the nanoscale, as revealed by direct analysis [10]–[17], leads to the formation of a coherent correlated state (CCS) of deuterons. The potential existence of such quantum states was initially contemplated by Schrödinger and Robertson [18], [19]. The creation of CCS is intricately tied to the optimal phase synchronization of quantum states of a particle in a superposition state within a nonstationary potential well.

When a deuteron is localized within a typical interatomic interval $a \approx 2 \text{ \AA}$ or within a nanocrack of size $a \approx 10 - 20 \text{ \AA}$, the energy fluctuation in CCS surpasses the value

$$\delta E \geq G^2 \hbar^2 (2N + 1) / 8M (\delta x)^2 \geq 10 - 30 \text{ keV}. \quad (16)$$

Here, $\delta x \approx a/2$, $G \equiv 1/\sqrt{1-r^2} \approx 10^3 - 10^4$ is the realistic coefficient of correlation efficiency, and $N = 0, 1, 2, \dots$ is the number of the energy level of the deuteron in this potential well before the impact of the shock wave. At room temperature of the target $N \approx 5 - 50$ for interatomic potential wells or nanocracks in titanium, respectively.

The substantial increase in particle energy fluctuation δE during CCS formation is linked to the Schrödinger-Robertson uncertainty relation [18], [19] and is associated with the further development of this method applied to nuclear physics problems [11]–[17].

It is very important that in CCS formed during modulation of a potential well, both the amplitude δE of kinetic energy fluctuations and the duration δt of these fluctuations increase very significantly compared to the “usual” Heisenberg uncertainty relation $\delta t \geq \hbar/\delta E$. It was shown [16], [17] that without such increase of δt , no nuclear reactions would be possible.

Our experiments [20] have unveiled a significant impact of thermal waves on the structure of distant crystalline targets. In this study, we have examine the phase composition and structure of one titanium (Ti) sample and two Ti samples saturated with deuterium (D) at 150%, both before and after irradiation with thermal waves. The investigation was conducted using an X-ray diffractometer with a rotating copper anode. Notably, a five-minute irradiation of two identical $TiD_{1.5}$ samples and one pure Ti sample with thermal waves at a distance of 20 cm resulted in a substantial compression of their crystal lattices, as detailed in Table 1.

Table 1. Deformation (compression) of a crystalline target after irradiation by a thermal wave

Test sample	Crystal lattice period, Å (before irradiation)	Crystal lattice period, Å (after irradiation for 5 minutes)
<i>Ti</i>	2.939 and 4.691	2.927 and 4.669
<i>TiD</i> _{1.5} (1)	4.404	4.396
<i>TiD</i> _{1.5} (2)	4.403	4.399

It is evident that local and instantaneous (with subsequent return) deformations of the crystal lattice at the locations of nanocracks and impurity deuterium nuclei could exceed these values. These findings affirm the significant influence of the irradiation process on the dynamic microstructure of the irradiated targets.

3.2. Stimulation of He^3 Fusion in a Remote *TiD* Target

Experiments were conducted to implement the $d + d = He^3 + p$ channel of the (dd)-reaction (15), leading to the formation of He^3 nuclei. The experimental setup, as illustrated in Fig. 1, utilized a *TiD* target (length – $L = 10$ mm, diameter – $D = 7$ mm, saturation $\sim 150\%$) and track detectors. The titanium sample was saturated using a standard method in a special closed chamber at a high pressure of about 1 atm of gaseous deuterium and a temperature of 300–350°C. Repeat studies using an X-ray diffractometer after 0.5 year, 1 year and 3 years showed that the original high density of deuterium in the target remained unchanged.

The *TiD* target was positioned approximately 20 cm away from the cavitation chamber.

For He^3 track analysis, a plastic CR-39 type detector made of polycarbonate (polyallyl diglycol) with a density of 1.3 g/cm³ and a thickness of 1 mm (“TASTRAKtm” detector from Track Analysis Systems Ltd, Bristol, UK) was employed. Standard experimental conditions involved placing the detector 5 mm away from the surface of the target, subject to the thermal wave for specific durations (20 and 40 minutes). Post-irradiation, the detector underwent 6.25-M etching using a NaOH solution for 3.5 hours at a temperature of 80°C.

The image of tracks was photographed using an Olympus BX-51 optical microscope with the Image Scope M program.

In Fig. 2a, a photograph of a track detector is presented, positioned 5 mm behind the reverse end surface (relative to the thermal wave source) of the cylindrical *TiD* target.

Fig. 2b shows a photograph of a fragment of a similar flat track detector located parallel to the side surface of the same cylindrical *TiD* target at a distance of 5 mm.

Both detectors were exposed for the same time (40 minutes). In Fig. 2a and 2b, the directions of movement of heavy charged particles (nuclei 3) when they hit the surface of the track detector are indicated by arrows. There were no traces of tracks on the back of the track detector.

For control purposes, Fig. 2c presents a segment of a comparable track detector irradiated with a reference “triplet” alpha radiation mixed source: U^{233} , Pu^{238} , and Pu^{239} . The energies of alpha particles He^4 emitted during the decay of these isotopes are respectively equal to 4.679 MeV, 5.593 MeV and 5.157 MeV [21].

Another proof of the reliability of the implemented nuclear fusion of He^3 nuclei is the axial symmetry of the tracks on Fig. 2b, which corresponds to the cylindrical shape of the *TiD* target and the spatial symmetry of the thermal waves that irradiate this target. In the hypothetical presence of background alpha-like radiation (for example, in the presence of radon gas), the orientation of these tracks would be completely random. In addition, similar track detectors stored in the same laboratory, in the absence of such irradiation by a thermal wave, remain without any tracks on both its surfaces even during long-term storage.

A detailed analysis of the experiment on the fusion of He^3 nuclei in a remote target under the influence of a thermal wave is presented in Table 2.

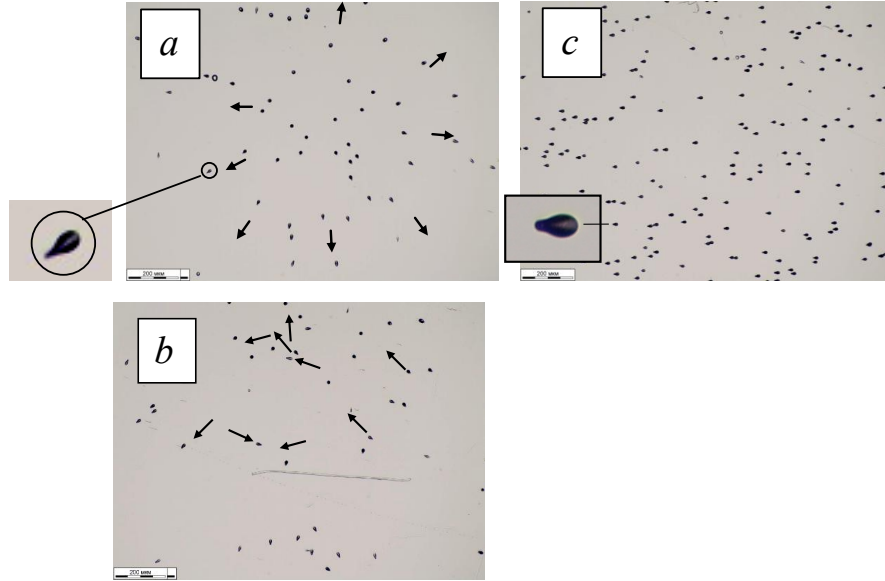


Figure 2. a) Track analysis showing the movement of heavy charged particles produced in a distant *TiD* target the opposite end surface of which was irradiated with thermal radiation for 40 minutes. b) Photograph of a fragment of a similar flat track detector located parallel to the side surface of the same cylindrical *TiD* target. c) Photograph of a similar track detector irradiated with a reference alpha emitter based on a three radionuclides: U^{233} , Pu^{238} , Pu^{239} . The directions of movement of nuclei 3 when they hit the surface of the track detector are indicated by arrows.

Table 2. Measured and estimated parameters of alpha particle fusion stimulated thermal wave

Thermal wave irradiation of the <i>TiD</i> target	Number of registered alpha-tracks	Full flux of alpha particles on the reverse surface <i>S</i> of the target	The total number of $d(d,p)He^3$ reactions in target volume upon irradiation with a thermal wave	The rate of stimulated nuclear alpha particle fusion during thermal wave irradiation of the target
$T_0 = 40$ minutes	$N_0 = 52$	$N_s \approx 1000$ (taking into account absorption in air and in near-surface layer of <i>TiD</i> target)	$N_0 \approx \frac{2N_s L}{\langle l_{He^3} \rangle} \approx 2 \cdot 10^7$ (estimation)	$\eta_{H^3} = \frac{N_0}{LSn_{H^2}T_0} \approx 2.2 \cdot 10^{-19}$ created He^3 nuclei/s· H^2 nucleus

Here $\langle l_{He^3} \rangle \approx 1.25 \mu m$ is He^3 nucleus free path in *Ti*; $n_{H^2} = 1.5 \cdot n_{Ti} \approx 8.2 \cdot 10^{22} cm^{-3}$ is the concentrations of *D* atoms in *TiD* target; $S = 0.38 cm^2$ is the surface of the target's back end.

3.3. Stimulation of Tritium Fusion in a Remote *TiD* Target

An evaluation of the efficiency of the alternative (dd)-reaction $d + d \rightarrow H^3 + p$ was conducted on the same samples after a period of $t_0 = 6$ months following irradiation with a temperature wave for 20 or 40 minutes. This delay in measurement was chosen to ensure the presence of long-lived synthesized H^3 nuclei. This analysis utilized a radioluminescence method, accounting for the spatial position and beta activity of the resulting H^3 nuclei with a half-life $T_{1/2} = \tau_T \ln 2 = 12.3$ years in irradiated *TiD* targets.

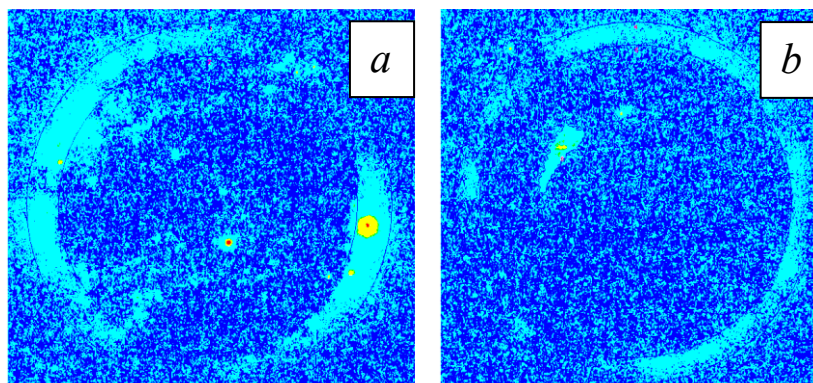


Figure 3. Photographs of radioluminograms formed upon irradiation of radioluminogram plate with electrons created during the beta decay of tritium, which was synthesized by the action of a temperature wave on distant *TiD* targets for 40 minutes (a) and 20 minutes (b).

Table 3. β^- activity of *TiD* targets irradiated 6 months ago by the thermal waves

Thermal wave irradiation time	Duration of rendering by <i>HeNe</i> laser beam	Surface of active radioluminogram,	Total surface directional β^- activity Q_s, Bk (toward detector)
$T_0 = 40 \text{ min}$	65 hours	1.05 cm^2	163.5
$T_0 = 20 \text{ min}$	65 hours	0.88 cm^2	40.5

Fig. 3 presents photographs of two radioluminograms illustrating the spatial distribution and concentration of synthesized tritium in the *TiD* target area near the rear (end) surface.

Fig. 3a corresponds to the target irradiated for 40 minutes, and Fig. 3b corresponds to 20 minutes.

The absence of radioactive background in the laboratory is also confirmed by the result that the concentration of registered active centers on the back side of the *TiD* targets increases approximately proportionally to the duration of irradiation with a thermal wave (20 and 40 min).

These radioluminograms result from *HeNe* laser imaging (photostimulated luminescence) of latent images formed in irradiated phosphor plates by β^- during $H^3 = He^3 + \beta^- + \tilde{\nu}$ decay. The radioluminogram plate consists of a $50 \mu\text{m}$ thick luminescent layer and a $410 \mu\text{m}$ thick substrate. The luminescent layer comprises a mixture of phosphor $BaFBrEu^{2+}$ and crystal-binding phosphor polymer ($C/H/N/O = 8/12/2/1$) in a composition ratio of 20:1 by weight. The substrate consists of a layer of polyethylene terephthalate with a thickness of $250 \mu\text{m}$, covering the base of ferrite $160 \mu\text{m}$ thick. Specific radiation dose determination is achieved by comparison with a special standard Amershan reference plate containing 16 known levels of tritium activity. Upon exposure to beta particles emitted by tritium, electronic *F* centers and hole centers ($Eu^{2+} \rightarrow Eu^{3+}$) are formed. This system of centers creates a latent distribution image of tritium on the imaging plate.

After contact with the radioactive sample under study, the plate is placed in the reader, where, under the action of a focused laser beam, photostimulated luminescence occurs sequentially at each point. Under the influence of *HeNe* laser radiation in the red range ($\lambda \approx 633 \text{ nm}$), electrons are released from F-centers and annihilate with Eu^{3+} hole centers, forming Eu^{2+} ions in the excited state, which, in less than one millisecond, return to the ground state. During this process, radiation quanta are emitted with a wavelength belonging to the blue-violet range of the visible spectrum ($\lambda \approx 390 \text{ nm}$). These quanta enter a photomultiplier through a light guide and are recorded as an analog electrical signal, subsequently converted into a digital signal.

The β^- activity parameters recorded from these radioluminograms are presented in Table 3.

Table 4. Parameters of tritium fusion in *TiD* target irradiated with a thermal wave

Thermal wave irradiation time	Total volume beta activity (estimated value), Bk/TiD target	Total concentration of created tritium nuclei (estimated value), cm^{-3}	The rate of total tritium fusion by thermal wave in $d+d=H^3+p$ reaction, $cm^{-3} s^{-1}$
$T_0 = 40 \text{ min}$	$Q_{total} \approx \frac{2Q_{SL}}{\langle l_b \rangle} \approx 10^7$	$n_{total} = \frac{Q_{total} \tau_T}{L \cdot Se^{-T_0/\tau_T}} \approx 4 \cdot 10^{15}$	$\alpha = \frac{n_{total}}{T_0} \approx 1.7 \cdot 10^{12} cm^{-3} s^{-1}$
$T_0 = 20 \text{ min}$	$Q_{total} \approx 2.5 \cdot 10^6$	$n_{total} = 10^{15}$	$\alpha \approx 0.43 \cdot 10^{12} cm^{-3} s^{-1}$

The distinctive non-uniform distribution of activity on the surface of the investigated *TiD* was observed during both intermediate analyses of the radioluminographic plate after 19 *hours* (control) and after 65 *hours*. This observation validates the stable distribution of fusion regions and beta activity in the same locations, aligning with the microstructure of the target. It has been demonstrated that the mean free path of electrons formed during beta decay of tritium in a flat layer of titanium crystal corresponds to $\langle l_\beta \rangle \approx 0.4 - 0.5 \mu m$.

The final parameters of tritium fusion stimulated by a thermal wave are presented in Table 4.

These data correspond to the rate of stimulated nuclear tritium fusion

$$\eta_{H^3} = \begin{cases} T_0 = 40 \text{ min}, & \alpha_{40}/n_{H^2} \approx 2.1 \cdot 10^{-11} \\ T_0 = 20 \text{ min}, & \alpha_{20}/n_{H^2} \approx 0.52 \cdot 10^{-11} \end{cases} \text{ created } H^3 \text{ nuclei/sec} \cdot H^2 \text{ nucleus.} \quad (17)$$

A significant nonlinear (quadratic) increase in the total concentration n_{total} of LENR and a linear increase in the rate of these reactions with an extended duration of the temperature wave action indicates an active nonlinear influence of this wave on the conditions for LENR implementation. Such irradiation not only stimulates LENR but also establishes conditions for more efficient LENR, potentially due to the formation of additional nanocracks in the titanium matrix with deuterium or deformation of existing nanocracks (see section 2.1 above).

4. Conclusions

The results obtained demonstrate that undamped temperature waves with frequencies (12), formed during cavitation of a water jet, can propagate over long distances without absorption. These frequencies are determined by the local thermal relaxation time τ in the material medium through which these waves travel.

These waves can effectively stimulate LENR in distant targets. The experiments conducted to stimulate dd-fusion in a distant *TiD* target using such waves reveal that the probability and rate η_{H^3} of tritium fusion in the $d + d = H^3 + p$ reaction are approximately 10^8 times higher than the probability and rate η_{He^3} of He^3 fusion and neutron generation in the alternative $d + d = He^3 + n$ reaction. These findings illustrate a fundamental distinction between LENR and similar reactions involving particles with high real (not virtual) energy. Additional differences between LENR and hot fusion were discussed in [13], [14], [22]–[24].

The reliability of the experimental results obtained is confirmed by several factors. In particular, plastic CR-39 type detectors are stored in the laboratory for a fairly long time, and they remain completely clean. The absence of radioactive background in the laboratory is also confirmed by the result that the concentration of registered active centers on the back side of the *TiD* targets increases approximately proportionally to the duration of irradiation with a thermal wave (20 and 40 *min*). This is clearly seen when comparing Fig. 3a and 3b.

The same effect of direct dependence of the total number of registered particles on the surface of the track detector on the time of irradiation by a thermal wave occurs when studying the reaction with the formation of nuclei He^3 . Also convincing confirmation of the reliability of the results is the complete axial symmetry of the orientations of the tracks from He^3 nuclei (Fig. 2a), which is associated with the axial symmetry of both the source of thermal waves and the *TiD* target when recording tracks behind the rear surface of this target.

The results of additional studies of the nuclear fusion under consideration (including the possibility of alpha particle He^4 formation in the process of implementing the third reaction (15)) will be discussed in the future after the completion of additional experiments.

References

- [1] V.I.Vysotskii, V.B.Vassilenko, A.O.Vasylenko. Generation and propagation of undamped temperature waves under pulse action on a target surface, *J. Surface Invest.*, **8** (2014) 367–373.
- [2] V.I.Vysotskii, A.A.Kornilova, A.O.Vasylenko, V.I.Tomak. Detection and investigation of undamped temperature waves excitation under water jet cavitation. *J. Surface Invest.*, **8** (2014) 1186–1192.
- [3] V.I. Vysotskii, A.A.Kornilova, A.O.Vasilenko. Observation and investigation of X-Ray and thermal effects at cavitation. *Current Science*, **108** (2015) 114–119.
- [4] V.I.Vysotskii, A.A.Kornilova, A.O.Vasylenko, T.B.Krit, M.V.Vysotskyy. On the long-range detection and study of undamped directed temperature waves generated during the interaction between a cavitating water jet and targets. *J. Surface Invest*, **11** (2017) 749–755.
- [5] V.I.Vysotskii, A.A.Kornilova, T.Krit, S.Gaydamaka. Generation and detection of undamped temperature waves at large distance in LENR related experiments. *J. Condensed Matter Nucl. Sci.* **29** (2019) 368–375.
- [6] A.A.Kornilova, V.I.Vysotskii, T. Krit, M.V.Vysotskyy, S.N.Gaydamaka. Study of the influence of remote undamped temperature waves on nuclear fusion, *J. Surface Invest.*, **14** (2020) No. 1, pp. 117–123.
- [7] V.I.Vysotskii, A.A.Kornilova, P.L.Hagelstein, T.B. Krit, S.N.Gaydamaka, M.V.Vysotskyy. Distant behind-screen action of undamped temperature waves (long-distance propagation, X-Ray generation, LENR stimulation), *J. Condensed Matter Nucl. Sci.* **33** (2020), 296–304.
- [8] W.M.Preston, Nuclear Reactions Involving Few Nucleons, Addison–Wesley, Reading, Massachusetts, 1962.
- [9] R.C.Johnson, Alpha Clustering and Nuclear Molecules”, *Reports on Progress in Physics*, 1982, Vol. **45** (1982) 625–683; DOI: 10.1088/0034-4885/45/6/002
- [10] V.I.Vysotskii, M.V.Vysotskyy. Features of correlated states and a mechanism of self-similar selection of nuclear reaction channels involving low-energy charged particles. *J. Exp. Theor. Phys.*, **128**, No. 6 (2019), 856–864.
- [11] V.I.Vysotskii, M.V.Vysotskyy, Coherent correlated states and low-energy nuclear reactions in non stationary systems. *European Phys. Jour. A*, **49** (2013), 99.
- [12] V.I.Vysotskii, S.V.Adamenko, M.V.Vysotskyy, Acceleration of low energy nuclear reactions by formation of correlated states of interacting particles in dynamical systems. *Annals of Nuclear energy*, **62** (2013), 618.
- [13] V.I.Vysotskii, M.V.Vysotskyy. Correlated states and transparency of a barrier for low-energy particles at monotonic deformation of a potential well with dissipation and a stochastic force. *J. Exp. Theor. Phys.*, **118**(4) (2014), 534.
- [14] V.I.Vysotskii, M.V.Vysotskyy. Coherent correlated states of interacting particles – the possible key to paradoxes and features of LENR, *Current Science*, **108** (2015), 524.
- [15] V.I.Vysotskii, M.V.Vysotskyy. Application of correlated wave packets for stimulation of LENR in remote targets, *J. Condensed Matter Nucl. Sci.*, **33** (2020), 305–313.
- [16] V.I.Vysotskii, M.V.Vysotskyy. Features of correlated states and a mechanism of self-similar selection of nuclear reaction channels involving low-energy charged particles, *J. Exp. Theor. Phys.*, **128** (2019), 856–864.
- [17] V.I.Vysotskii, M.V.Vysotskyy. Universal mechanism of LENR in physical and biological systems on the base of coherent correlated states of interacting particles. *Cold Fusion. Advances in Condensed Matter Nuclear Science*, Edd. by J.P. Biberian. Elsevier, 2020, CHAPTER 17, 333–370.
- [18] E.Schrödinger. Heisenbergschen Unschärfepinzip. *Ber. Kgl. Akad. Wiss.*, **S24** (1930) 296.
- [19] H.P.Robertson. A general formulation of the uncertainty principle and its classical interpretation, *Phys.Rev.A*, **35**, (1930), 667.
- [20] A.A.Kornilova, V.I.Vysotskii et al. The problem and implementation of sustainable generation of alpha particles by TiD located in a thermal wave field, *Engineering physics*, #5, (2018), 14–22.
- [21] Stephanie Cockcroft, Peter E. Dyer, Craig S. Moore, Christopher D. Walton 2009; <https://www.researchgate.net/publication/251891483/figure/fig6/AS%3A668690219560964%401536439580273/SEM-images-of-the-tracks-etched-in-CR39-exposed-to-the-alpha-source-and-chemically-etched.ppm>

- [22] V.I.Vysotskii, M.V.Vysotsky. Self-controlled flashing nuclear fusion in stationary magnetized low-temperature plasma. *Fusion Sci. and Technology*, 79:5 (2023), 537–552.
- [23] V.I.Vysotskii, M.V.Vysotsky. Manifestations in nature of self-controlled quasi-stationary nuclear fusion into magnetized low-temperature hydrogen plasma. *Frontiers Materials, Sec. Quantum Materials*, vol.11 (2024). <https://doi.org/10.3389/fmats.2024.1502051>.
- [24] V.I.Vysotskii, M.V.Vysotsky. Current status of the coherent correlated states for explanation of LENR. *J. Condensed Matter Nucl. Sci.* 39 (2025) 165–184.